UDC 551.46.01:551.465.7:551.588.5

CLIMATE AND THE OCEAN CIRCULATION

III. THE OCEAN MODEL

KIRK BRYAN

Geophysical Fluid Dynamics Laboratory, ESSA, Princeton, N.J.

ABSTRACT

The ocean model used in a calculation of the earth's climate is described in detail. Compared with earlier numerical models used in ocean circulation studies, the present model includes several new features. Temperature and salinity are treated separately. Density is calculated with an accurate equation of state for sea water. The model also includes a method for calculating the growth and movement of sea ice.

Due to the very slow adjustment of the deep water in the ocean model, a numerical integration extending over the equivalent of a century fails to reach a climatic equilibrium. At the termination of the run, the surface layers of the ocean show little change with respect to time, but the average heating rate for the ocean as a whole is 2° per century. The salinity patterns at the termination of the run are highly realistic compared to observations. A halocline forms in the Arctic Zone and a surface salinity maximum is present in the subtropics. A weak salinity minimum at a depth of 1 km indicates an extensive water mass very similar to the Antarctic intermediate water of the Southern Hemisphere. Poleward heat transport is found to be closely related to the intensity of the thermohaline circulation. A vertical mixing coefficient, κ, of 1.5 cm^2 sec^{-1} leads to very reasonable heat exchange with the atmosphere based on estimates of the heat balance of the North Atlantic.

The calculation indicates that the thermal "relaxation" time of the ocean is too long for a numerical integration of the time-dependent equations to be a practical method of finding an equilibrium solution, and new methods should be sought for future calculations of this type.

CONTENTS

1. INTRODUCTION

A numerical experiment has been carried out to investigate climate by means of a joint atmosphere-ocean numerical model. The present paper is the third of three papers describing this calculation in some detail. The numerical experiment is a first attempt to compute an equilibrium climate based on relatively complete formulations of the atmospheric and oceanic general circulations. The atmospheric model includes a quite detailed description of the surface heat and water balance. The horizontal resolution of the numerical grid in the atmosphere and ocean model is of the order of a few hundred kilometers. With respect to the vertical, calculations are carried out at nine levels in the atmosphere and at five levels in the ocean. The levels are spaced in a uniform way to give maximum resolution near the air-sea interface. Most of the essential factors in climate have been well known since the early part of the 20th century, but the relative importance of these factors remains a matter of speculation. The large number of actively competing theories to explain the ice ages supports this view. The motive for this numerical experiment is the pressing need for a more quantitative understanding of climate.

The atmospheric model described by Manabe (1969*a*, *b*) in parts I and II is the outgrowth of earlier investigations by Phillips (1956) and Smagorinsky (1963) in which the methods of numerical weather forecasting have been applied to the study of the general circulation of the atmosphere. Numerical studies of ocean circulation are not as far advanced. A valuable point of departure for the formulation of numerical models of a baroclinic ocean exists in the thermocline investigations of Lineykin (1955), Robinson and Stommel (1959), and Welander (1959); and pioneering work in numerical modeling of the thermohaline circulation has been carried out by Sarkisyan (1962) in the Soviet Union. The present ocean model is based on two earlier studies carried out at the Geophysical Fluid Dynamics Laboratory of ESSA (Bryan and Cox, 1967 and 1968*a*, *b*). The reader is referred to these studies for details on the numerical methods, and an analysis of the dynamic behavior of the model.

In the previous calculations carried out by Bryan and Cox (1967 and 1968*a*, *b*), the effects of salinity and temperature are combined in an "apparent temperature," but a separate treatment is necessary in the present case where we wish to study the details of the global heat and water balance. Another new feature required by a model of climate is a method of computing the formation of sea ice. At high latitudes the formation of sea ice is a

very important factor in creating an insulating shield between the ocean and atmosphere. Once a heavy layer of sea ice is formed, the exchange of heat and moisture across the air-sea interface is greatly reduced. Sea ice, like snow cover over land, has a rather unique positive climatic feedback, since it tends to accentuate any tendency for the climate to become colder. This effect has long been recognized by climatologists (Brooks, 1926).

In an advanced stage of the analysis of the results, it was found that an error is present in the calculations of the joint model. An extraneous factor of $\cos\phi$ gives a fictitiously low value of the wind stress applied to the ocean at higher latitudes. To test the effect of this error, a 30-yr extension of the final run is carried out with the error eliminated. The results are discussed in the appendix.

2. THE BASIC EQUATIONS

The ocean model is very similar to that studied by Bryan and Cox (1967 and 1968*a*, *b*). The essential simplifications of the model are: the hydrostatic assumption, the Boussinesq assumption with respect to density variations, and an implicit treatment by a "turbulent viscosity" hypothesis for motions too small to be resolved by the numerical grid. In order to introduce more geophysical detail in the present model, several features have been added. These new features include 1) a complete equation of state, allowing temperature and salinity to be treated separately, 2) a more exact formulation of the lateral diffusion of momentum in spherical geometry, and 3) upper boundary conditions permitting the formation of sea ice.

Let $\mathbf{v}$ be the horizontal velocity vector, and ∇ the horizontal grad operator. The equation of motion and the hydrostatic relation may be written,

$$\mathbf{v}_t+\mathbf{v}\cdot\nabla\mathbf{v}+w\mathbf{v}_z+(2\Omega+\dot{\lambda})\sin\phi\mathbf{k}\times\mathbf{v} =-\nabla(p/\rho_0)+\kappa\mathbf{v}_{zz}+\mathbf{F} \quad (1)$$

and

$$\rho g=-p_z \quad (2)$$

where ϕ is the latitude, and $\dot{\lambda}$ is the angular velocity relative to the rotating coordinate system. κ is the coefficient of turbulent mixing in the vertical. $\mathbf{F}$ is a horizontal body force due to lateral mixing. In terms of a spherical coordinate system,

$$F^{\lambda}=\frac{A_M}{a^2}\left[\nabla^2 u+(1-\tan^2\phi)u-2\frac{\tan\phi}{\cos\phi}v_{\lambda}\right] \quad (3)$$

and

$$F^{\phi}=\frac{A_M}{a^2}\left[\nabla^2 v+(1-\tan^2\phi)v+2\frac{\tan\phi}{\cos\phi}u_{\lambda}\right] \quad (4)$$

where

$$\nabla^2(\ )=\sec^2\phi(\ )_{\lambda\lambda}+\sec\phi\,(\cos\phi\,(\ )_{\phi})_{\phi}. \quad (5)$$

The correct form for the friction terms for the nonisotrophic case in which the level of vertical mixing differs from the horizontal mixing has been derived by Saint-Guilly (1956). A_M is the coefficient of lateral mixing for momentum taken to be 10^8 cm^2 sec^{-1}.

The equation of continuity is

$$w_z+\nabla\cdot\mathbf{v}=0. \quad (6)$$

The conservation equations for temperature and salinity below the surface and under conditions of stable stratification are:

$$(T,S)_t+\mathbf{v}\nabla(T,S)+w(T,S)_z=\kappa(T,S)_{zz}+A_H\nabla^2(T,S). \quad (7)$$

The effect of pressure on temperature is neglected in the present model, although this effect should be included in more detailed studies of ocean circulation. The lateral coefficient of turbulent diffusion in equation (7) is chosen to be 2.5×10^7 cm^2 sec^{-1}. This choice is dictated by the resolution of the numerical grid. A_H should be as small as possible in order not to obscure the lateral transfer of heat and salinity of ocean currents. A minimum level of A_H, however, is needed to suppress features of the temperature and salinity fields too small to be resolved by the numerical grid. A similar argument applies to the turbulent viscosity coefficient, A_M.

The vertical diffusion coefficient, κ, is in a somewhat different category. The exact physical process by which vertical exchange takes place within the thermocline is unknown. The effects of this mixing, however, can be quantitatively estimated by examining vertical profiles of water mass properties. Stommel and Webster (1962) estimate that κ lies in the range 0.1 to 1.0 cm^2 sec^{-1}. From a study of Pacific data for the lower thermocline, Munk (1966) obtained a value of 1.3 cm^2 sec^{-1}. In a numerical study somewhat like the present one, Bryan and Cox (1967) found that a value of κ of approximately 1 cm^2 sec^{-1} leads to ocean circulation solutions with realistic poleward heat transport and a realistic thermocline depth. Ideally, a series of numerical experiments should be carried out over a range of values of κ. Since this is not feasible for a computation of the scale of the present experiment, a single value of κ must be selected. The value chosen is 1.5 cm^2 sec^{-1}. It is then necessary to judge the appropriateness of this parameter value *a posteriori* from the solution of the numerical experiment.

Convective overturning in the ocean involves small-scale motion that cannot be resolved on a grid designed to cover an entire ocean basin. Convection is therefore handled implicitly by imposing a constraint. This constraint cannot be easily expressed in analytic form, but is applied as follows: if equation (7) predicts an unstable stratification at any given time step, the predicted values of temperature and salinity are adjusted so that the vertical gradients of the temperature and salinity vanish. The temperature and salinity of the water column are exactly conserved during the adjustment process. An exception to this rule occurs only when a fixed temperature is imposed at the surface through the upper boundary condition. If instability is predicted adjacent to the surface in that case, the temperature is set equal to the fixed surface value. The numerical procedure is described by Bryan and Cox (1968*a*, p. 949).

The equation is of the general form,

$$\rho=\rho(T,S,p'). \quad (8)$$

A convenient formula for equation (8) due to Eckart (1958) is adopted,

$$\rho=\frac{p'+p_0}{1.000027[\lambda+\alpha_0(p'+p_0)]}. \quad (9)$$

Here ρ is given in gm cm^{-3} and p' is the total pressure in atmospheres. The parameters, p_0, α_0, and λ are defined as

$$\alpha_0=0.698,$$

$$\lambda=1779.5+11.25T-0.0745T^2-(3.8+0.01T)S, \quad (10)$$

and

$$p_0=5890+38T-0.375T^2+3S.$$

T and S are given in degrees Celsius and parts per thousand, respectively. In the present model, p' is approximated by the static pressure of a resting ocean of uniform density, ρ_0.

$$p'=\frac{\rho_0 g|z|}{1.013\times10^6}+1.0. \quad (11)$$

The numerator of the first term on the right of equation (11) is given in cgs units.

The basin is bounded by two meridians 60° of longitude apart. Symmetry is assumed at the Equator, and a zonal wall is placed at a latitude of 65°. The basin has a uniform depth of 4 km. At the lateral walls,

$$\mathbf{v}=(T, S)_n=0,$$

at $$\lambda=\lambda_0, \lambda_0+60°,$$

and $$\phi=\pm65° \quad (12)$$

where $(\ )_n$ denotes the local derivative with respect to the coordinate normal to the wall.

At the ocean bottom,

$$w=(\mathbf{v})_z=(T, S)_z=0, z=-4 \text{ km}. \quad (13)$$

At the surface,

$$w=0$$

and

$$(\mathbf{v})_z=\tau^*(\phi, \lambda). \quad (14)$$

The surface boundary conditions on temperature and salinity will be specified later in connection with a description of the ice pack model.

3. ARRANGEMENT OF THE NUMERICAL GRID AND INITIAL CONDITIONS

The numerical method is exactly the same as that described in detail by Bryan and Cox (1968*a*, *b*). The variables $\mathbf{v}$, T, and S are specified at each grid point at every time level. Grid points occur at five levels, placed at 67, 100, 300, 1,000, and 3,000 m below the surface. The horizontal arrangement of points is shown in figure 1. The grid points are laid out in even intervals in the y-direction with respect to a Mercator projection. Except

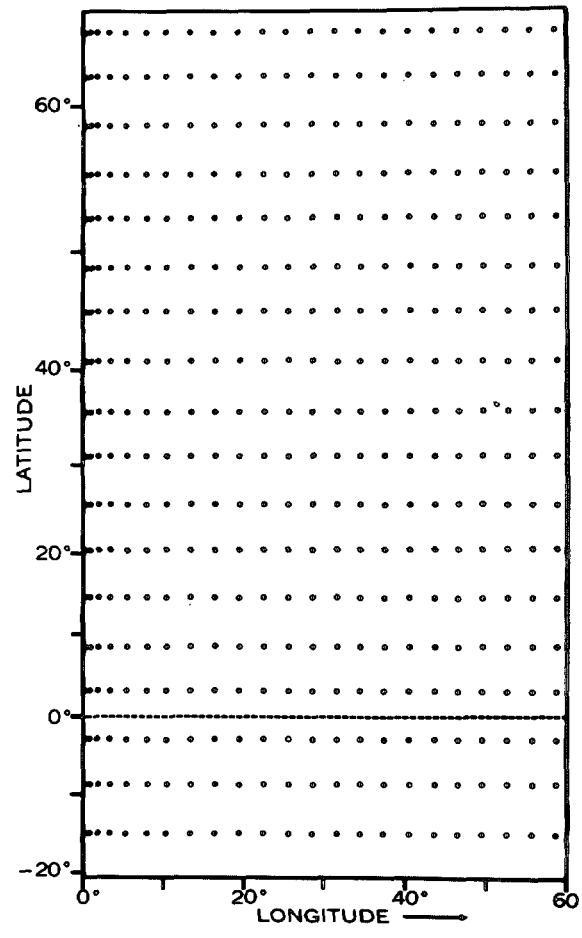

FIGURE 1.—Distribution of grid points in the horizontal plane. Note the extra resolution near the western boundary.

for the final run at high resolution, grid points are about 6° of latitude apart, with much smaller intervals at high latitudes. A variable spacing is used in the east-west direction. The grid points are 3° of longitude apart in the interior of the basin, but less than 1° apart near the western boundary. This arrangement allows for a better resolution of the western boundary current.

At the start of the first run, the ocean is at complete rest and surfaces of constant temperature and salinity are horizontal. The initial distribution of T and S with respect to the vertical is shown in table 1. The choice indicated in table 1 is somewhat arbitrary. A stable arrangement is chosen which has a thermocline depth approximately equal to that which would be predicted from thermocline scale theory (Stommel and Veronis, 1957). The bottom water has a temperature considerably colder than observed for our present climate. This was chosen to correspond with the very low surface temperature specified as a surface boundary condition at the start of the numerical integration.

4. PACK ICE MODEL

Pack ice forms a significant shield that reduces the free interaction of the ocean and atmosphere. It also provides a mechanism that, in conjunction with water vapor transport in the atmosphere, provides sources and

TABLE 1.—*Vertical distribution of T and S at the start of the first run*

$-z(m)$	67	100	300	1000	3000
T (°C)	26.0	18.0	12.0	2.5	−1.8
S (‰)	33.70	33.80	33.90	34.58	34.58
ρ (gm/cm³)	1.02223	1.02439	1.02570	1.02760	1.02796

sinks of fresh water at different locations on the ocean surface. At high latitudes, the transport of ice is as important a factor in the salt balance as the evaporation-precipitation cycle.

A substantial amount of information based on field observations and laboratory measurements is available on the local freezing and thawing of sea ice. Rather little is known, however, about the mechanisms of sea ice transport. While the balance of forces acting on a single, isolated ice floe can be formulated in terms of the stresses exerted by winds and currents, the problem is greatly complicated by frequent collisions with neighboring ice floes. In regions of particularily heavy ice concentrations something analogous to a logjam takes place, and all movement ceases. Recently an interesting attempt has been made to formulate the interaction of ice floes in terms of a large-scale "ice viscosity" (Campbell, 1965). However, this analogy does not relate many important aspects about the movement of floating ice, and a theory more closely based on the physics of ice movement is very much needed.

The present model bypasses the more difficult aspects of this problem. It is designed to take into account ice transport only insofar as it affects the large-scale heat balance. An effort has been made to introduce as few unknown parameters as possible, even where this may lead to the sacrifice of important geophysical detail. The principle simplifications of the pack ice model are:

1) Local freezing is proportional to the difference between heat lost to the atmosphere at the ice surface and heat supplied to the lower surface of the ice pack by ocean currents.

2) Heat loss through cracks in the ice pack is neglected, as well as the insulating effect of new snow. The ice is assumed to have a uniform conductivity equal to that of pure ice (5×10^{-3} cal/cm² sec). Measurements by Malmgren (1927) indicate that more than 1 m below the surface natural sea ice closely approaches pure ice in its conductivity.

3) The heat capacity of the ice itself is neglected. To take this factor into account, a multilevel model like that proposed by Untersteiner (1964) would be required.

4) Sea ice is advected with the mean speed of currents in the first 100 m below the ocean surface, except when the ice exceeds a critical thickness of 3 m. When this thickness is exceeded, the ice is assumed to lock and all motion by large-scale advection ceases.

5) Ice is mixed laterally by a turbulent diffusion, which has the same level as that used in the equations for temperature and salinity.

6) Malmgren (1927) observed that summer melt water penetrated right through the ice pack. Accordingly, it is assumed that any rain falling on the ice pack penetrated directly to the ocean below. On the other hand, snowfall directly augments the ice thickness.

7) The salt content of the ice pack is neglected.

To express the model in terms of an equation for the growth of ice, the following variables are defined:

I=ice thickness,
I_c=critical ice thickness for advection (3 m),
$\mathbf{V}$=average velocity for $0>z>-67$m,
k=thermal conductivity (5×10^{-3} cal/cm² sec),
ρ_I=density of sea ice,
L_f=latent heat of freezing,
ϵ=coefficient of heat transfer, determined empirically from experiments by Assur and Weeks (1964), $\epsilon=2.93\times10^{-3}$ cal/cm² sec,
R_n^*=rainfall,
S_n^*=local snowfall,
E^*=sublimation or evaporation,
T^*=temperature of the surface in contact with the atmosphere,
Q_b=heat supplied to the lower surface of the pack ice by the ocean, and
Q_a=heat supplied to the upper surface of the ice by atmosphere.

With the symbols defined above,

$$I_t=-\nabla(\delta_I\mathbf{V}I)+A_H\nabla^2I+S_n^*-E^*-(Q_a+Q_b)/\rho_IL_f \quad (15)$$

where

$$\delta_I=\begin{matrix}1 & I<I_c\\ 0 & I>I_c.\end{matrix}$$

The first two terms on the right-hand side of (15) represent the change of ice thickness due to lateral advection and lateral diffusion. The remaining terms account for the net accretion due to the effects of snowfall, sublimation, melting at the surface, and freezing on the undersurface of the ice pack. The freezing point of sea water (271.2°K) enters equation (15) through the definition of Q_a given in the following section.

Q_a is the heat exchange between the ice and the atmosphere and may be either positive or negative. Q_b is always zero or positive, since the underside of the ice is always as cold or colder than the water below.

5. BOUNDARY CONDITIONS AT THE UPPER SURFACE FOR HEAT AND SALINITY

The surface heat balance equation given by Manabe (1969*b*, section 2) is:

$$S^*+(\mathrm{DLR})_*=\sigma T_*^4+({}_VH)_*+({}_VLH)_*+({}_O\mathrm{H})_*. \quad (16)$$

The terms on the left are the incoming radiation, including the direct and diffuse components. The terms on the right are the outgoing radiation, heat loss due to upward sensible heat flux, heat loss due to evaporation, and heat loss to the underlying ocean, respectively.

We can identify Q_a of the previous section as,

$$Q_a = -({}_0\mathrm{H})_*. \tag{17}$$

For an ice surface, the heat flux associated with Q_a will be purely conductive, but in ice-free conditions Q_a will be associated with vigorous vertical mixing, partly associated with surface wave action.

Different boundary conditions are used with respect to surface temperature for stage I and stage II of the calculation. In stage I, the surface temperature over the ocean is specified initially as a function of latitude and longitude and held fixed during the entire computation.

Stage I—

$$T = T^*(\lambda, \phi), z = 0. \tag{18}$$

Where ice is present, the surface temperature of the ice is assumed to be at T^*, and the undersurface of the ice is held fixed at 271.2°K, which corresponds to the freezing point for sea water. The amount of heat transferred from the ocean to the atmosphere is governed by the thickness of the ice and its conductivity:

$$Q_a = \frac{k(T^* - 271.2)}{I + k/\epsilon}$$

and

$$Q_b = \frac{-\kappa}{z_0 - z_1}(271.2 - T_1). \tag{19}$$

A tendency for a thickening of the ice pack is indicated by equation (15) when T^* is less than 271.2°K. The term k/ϵ is equal to 1.7 cm for the parameters chosen in this study. Experiments indicate that for ice thickness less than k/ϵ, ice growth is nearly independent of thickness. For larger values of I, ice growth becomes inversely proportional to ice thickness. Thus as the ice pack builds up, an automatic feedback mechanism exists which slows down the rate of growth until it is balanced by other effects such as lateral advection.

Stage II—In stage II of the calculations, different boundary conditions on temperature are specified at the ocean surface. For ice-free conditions,

$$\kappa T_z|_{z=0} = Q_a^*. \tag{20}$$

In this case, T^* in the heat balance equation (16) is set equal to the average temperature of the upper layer, and Q_a^* is calculated as a residual term.[1] Since the various terms in the surface heat balance equation change with respect to time, Q_a^* is also a function of both time and the horizontal coordinates. From the standpoint of the ocean model, the boundary condition of stage II is much weaker than that of stage I. The ocean temperature structure is allowed to adjust itself quite freely.

The boundary conditions over the ice pack in stage II are necessarily quite complicated. The physical constraints that must be satisfied are: 1) the temperature of the surface of the ice pack cannot exceed the freezing point of fresh water, 273.1°K, and 2) the underside of the ice must remain at the freezing point of sea water, 271.2°K. To satisfy these constraints the following procedure is carried out at each time step. The temperature, T^*, at the surface of the ice pack is initially calculated from the surface heat balance equation (16) with Q_a determined by (19). If T^* calculated in this way turns out to be greater than 273.1°K, then it is adjusted to the freezing point. In this case, Q_a is calculated as a residual term in equation (16), following the same procedure used in stage I. Care is taken in formulating the numerical procedure that all heat exchanged with the atmosphere is completely accounted for in a corresponding change in water temperature or a certain amount of melting and freezing of ice.

The calculation of the salinity flux is done the same way in both stages I and II. In the present model the total volume of the ocean is kept fixed. Thus instead of water being removed during the evaporation process, as actually happens in nature, the amount of water remains the same and a flux of salt is calculated for the model. The reverse takes place when precipitation occurs in the model ocean. In "ice-covered" areas,

$$\left.\frac{\partial S}{\partial z}\right|_{z=0} = -S[R_n^* + (Q_a + Q_b)/\rho_I L_f], \tag{21}$$

while in "ice-free" areas

$$\left.\frac{\partial S}{\partial z}\right|_{z=0} = -S(R_n^* + S_n^* - E^*). \tag{22}$$

The physical interpretation of equation (21) is that in ice-covered areas the salinity change is due to precipitation, which percolates through the ice, and local melting. On the other hand, in ice-free areas salinity changes are brought about by the difference between precipitation and evaporation.

6. THE TIME DEPENDENT BEHAVIOR OF THE MODEL

A. STAGE I

As mentioned in the introduction, the numerical experiment with the ocean model is carried out in two stages. These stages make use of two sets of boundary conditions at the ocean surface. In stage I the wind stress, evaporation, precipitation, and surface temperature are prescribed. These fixed boundary conditions are based on the final results of the atmospheric computation described by Manabe (1969*a*) in part I of this study. These boundary conditions represent the equilibrium "climate" of the atmospheric model in the case of an inert ocean without lateral heat transport. In stage I of the ocean circulation, a symmetric condition is imposed at the Equator, while both hemispheres are included explicitly in stage II. At the start of stage I, temperature and salinity are horizontally uniform, and the system is in complete rest. The

[1] Setting the surface temperature in equation (16) equal to the average temperature of the top layer corresponds physically to the assumption of a homogeneous, strongly mixed layer extending from the surface down to 67 m.

vertical distributions of temperature and salinity that are chosen for initial conditions are given in table 1 in section 3.

Simplified scale considerations will help to clarify some aspects of the time-dependent behavior of the model. From the geostrophic current relation differentiated with respect to z, and the hydrostatic relation,

$$2\Omega \sin \phi v_z = \frac{-g}{a\rho_0} \sec \phi \, \rho_\lambda \tag{23}$$

where a is the radius of the earth. On the basis of equation (23), it is possible to define a scale velocity,

$$V^* = g\Delta\rho d/(2\Omega\rho_0 a) \tag{24}$$

where $\Delta\rho$ is the scale density difference prescribed by the surface boundary conditions, and d is the thickness of the thermocline. For typical values,

$$\begin{aligned} g &= 980 \text{ cm sec}^{-2}, \\ \Delta\rho &= 2.5\times10^{-3} \text{ gm cm}^{-3}, \\ 2\Omega &= 1.47\times10^{-4} \text{ sec}^{-1}, \\ d &= 4\times10^{4} \text{ cm}, \\ \text{and} \\ a &= 6.37\times10^{8} \text{ cm}. \end{aligned} \tag{25}$$

The scale velocity, V^*, is equal to 1 cm sec^{-1}. From continuity considerations,

$$V^*d/a = W^* = 6.3\times10^{-5} \text{ cm sec}^{-1} \tag{26}$$

where W^* is a scale velocity for vertical motion. Omitting the effects of lateral mixing and lateral advection, the following scalar relationship is based on the thermal equation,

$$\frac{\Delta T}{\Delta t} = -W^* \frac{\Delta T}{Z} + \kappa \frac{\Delta T}{Z^2}. \tag{27}$$

Here, Z is a measure of the depth and Δt is the time scale. On the basis of equation (27), it is possible to obtain two different measures of a time scale based on the two terms on the right-hand side. Based on the first term on the right,

$$\Delta t^* = Z/W^*. \tag{28}$$

Equating the term on the left to the second term on the right,

$$\Delta t^{**} = Z^2/\kappa \tag{29}$$

where Δt^* and Δt^{**} are the time scales associated with vertical advection and vertical diffusion, respectively. Numerical values are given in table 2. The exact numerical values given in table 2 are not significant. The main point is an indication of the difference between the time scale due to advection and a much longer time scale associated with vertical diffusion. The vertical advective time scale is shown to be of the order of decades, while the vertical diffusive time scale is of the order of centuries. Both these time scales must be important in the interaction of the ocean and atmosphere over longer periods of time. The advective time scale corresponds to the low-frequency, baroclinic geostrophic mode discussed by Veronis and Stommel (1956).

TABLE 2.—*Time scales depending on vertical advection and diffusion. Numerical values are based on* $W^* = 6.3\times10^{-5}$ *cm sec*$^{-1}$ *and* $\kappa = 1.5$ *cm*^{2} *sec*$^{-1}$.

$-Z$	(km)	0.5	1.0	2.0	3.0
Δt^*	(yr)	26	52	104	156
Δt^{**}	(yr)	52	210	840	1,900

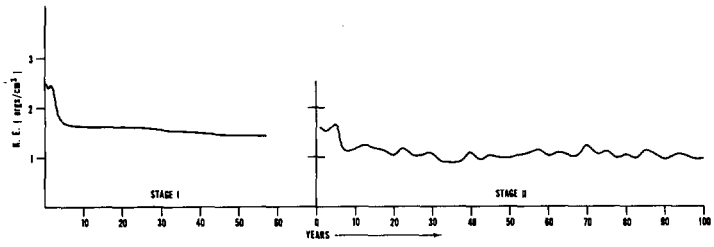

FIGURE 2.—Average kinetic energy per unit volume as a function of time.

The average kinetic energy per unit volume of the model is given as a function of time in figure 2. At the beginning of the run the kinetic energy jumps to a maximum value. Within a decade it settles down to a lower value, continuing to decrease very slowly during the latter part of stage I. Since the velocity and temperature fields must be closely connected to one another through the geostrophic relation, this behavior appears to contradict the estimates of time scales given in table 2. This point is discussed in a previous study by Bryan and Cox (1968*a*, *b*). The vertical advection time scale in table 2 is calculated for the vertical velocity of the interior. Along the lateral boundaries, however, much larger vertical velocities occur than in the interior. These vertical velocities along the boundary may in fact be several orders of magintude larger than those in the interior. As a result, the advective time scale at the boundary is very short. The curve of total kinetic energy reflects the very rapid response of the boundary currents to the initial conditions. The relatively small velocities in the interior only give a very small contribution to the total integral.

The time history of zonal averages of temperatures at the 67-, 300-, 1000-, and 3000-m levels is shown in figure 3a–d. In stage I, the response is rapid near the surface where Z in equation (29) is small. The temperature at 3000 m continues to change at a nearly steady, but slow rate.

The very low temperatures specified at the surface as a fixed upper boundary condition in stage I lead to a rapid growth of sea ice in the northern part of the model ocean. The total amount of ice as a function of time is shown in figure 4. Within the first decade of stage I, the total ice

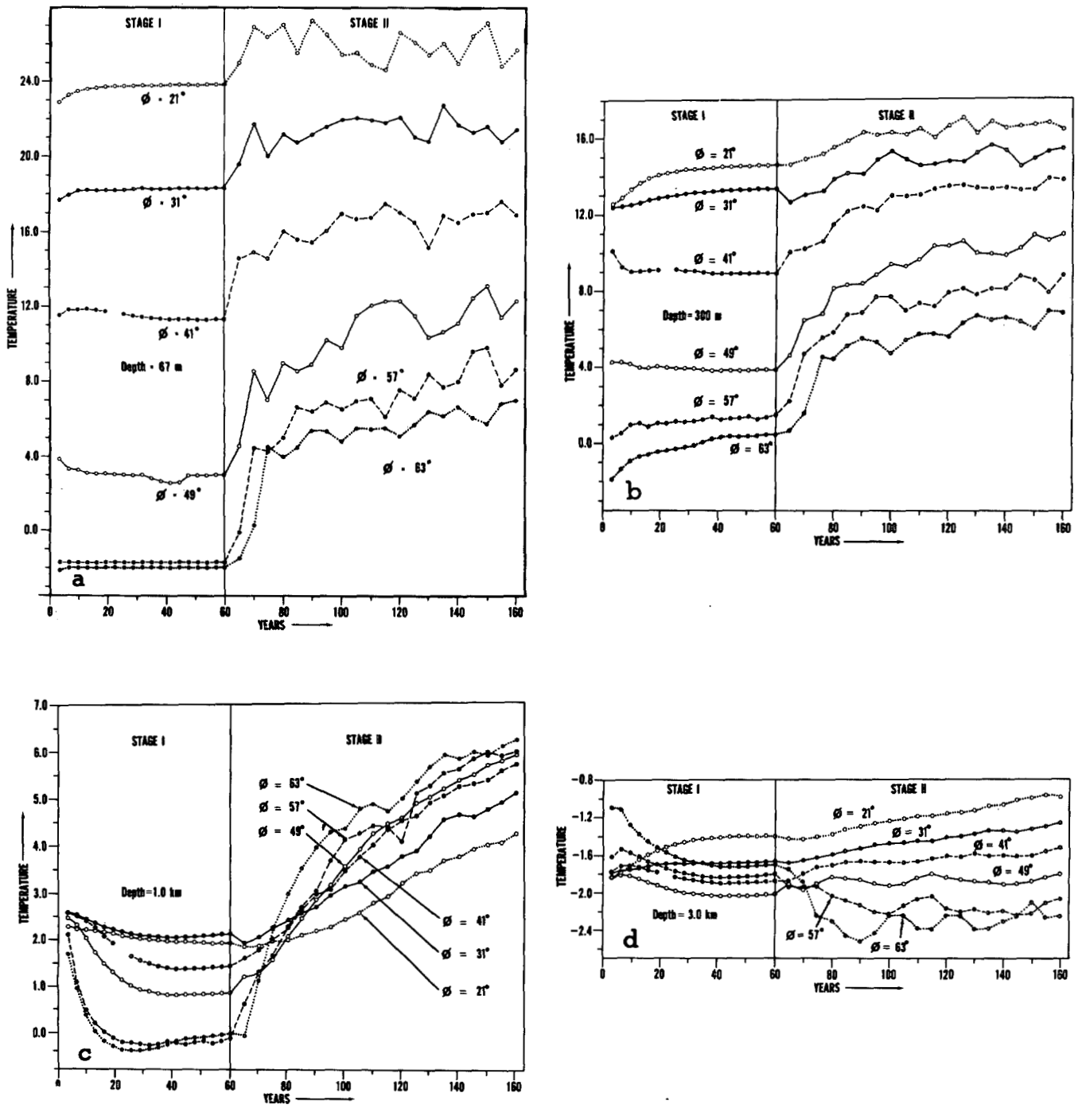

FIGURE 3.—Zonally averaged temperature at different latitudes as a function of time. Note the increase in the scale of the ordinate at greater depths.

steadies off to a nearly constant value of 10^{13} metric tons. A discontinuity arises at the beginning of stage II. The new boundary conditions at first cause an almost instantaneous increase in the total ice. The rise is so rapid that in figure 4 the ice appears to start out at a higher value in stage II. The rapid rise is followed by a gradual decrease, so that after the first decade of stage II all the ice has disappeared. From this point on, the ice pack ceases to be a factor in the climate of the model.

The pattern of the ice cover at the end of stage I is shown in figure 5. As might be expected, the ice cover is thickest near the continental boundaries and thinnest over the open ocean. The ice is pushed furthest to the north by the eastern branch of the counterclockwise sub-

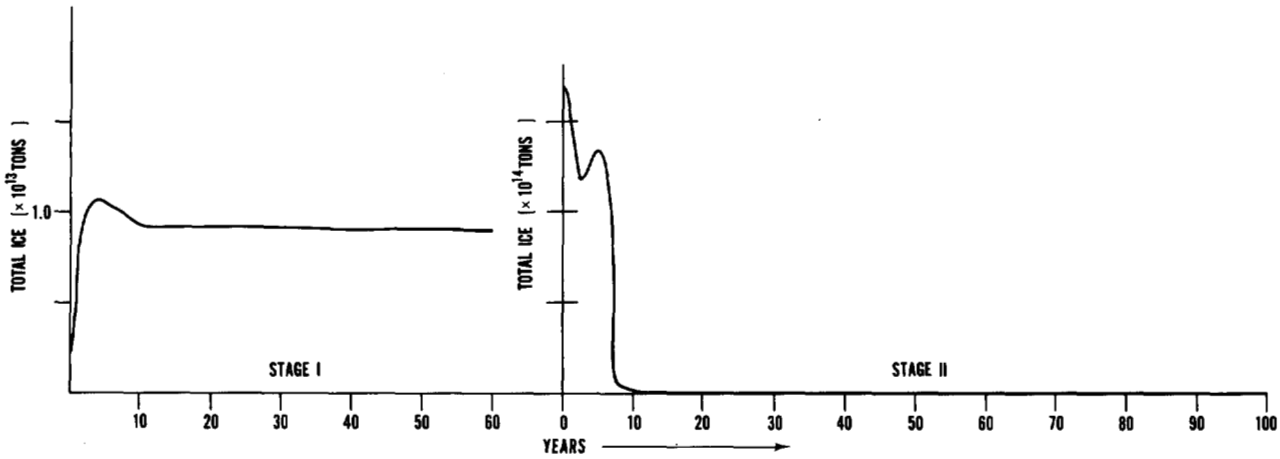

FIGURE 4.—Total amount of ice as a function of time.

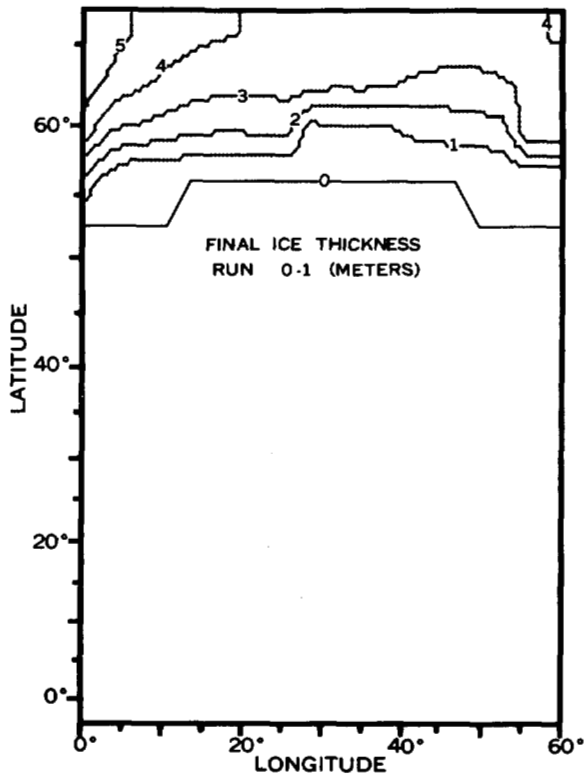

FIGURE 5.—Pattern of ice cover at the end of stage I.

arctic gyre. An important factor at the eastern boundary is the convergence of surface water. As the surface water converges and sinks, the ice tends to accumulate and thicken. In this area the ice "locking" parameter, δ_I, given in equation (15) plays an important role in limiting the accumulation of ice.

B. STAGE II

Calculations for the ocean model in stage II are extended to both hemispheres by removing the symmetry condition at the Equator. The boundary conditions at the upper surface of the ocean are also changed to allow a feedback to take place in a coupled ocean-atmosphere system.

The nature of the coupling between the models requires special explanation. The following is intended to supplement the discussion of the system given in part II by Manabe (1969*b*). The temperature at the surface is set equal to that of the first level in the ocean model at 67 m. This is equivalent to specifying that the mixed layer is 67 m deep. Let P^* be the total precipitation including both rain and snowfall. The vertical fluxes of heat, Q^*, the net vertical flux of water, $(E-P)^*$, and the vertical flux of momentum, τ^*, are determined by the atmospheric model. The radiation input in the atmospheric model is based on the seasonally averaged isolation. Thus, certain climatic features which depend on seasonal changes are omitted. The surface temperature T^* serves as a lower boundary condition for the atmospheric model, while Q^*, $(E-P)^*$, and τ^* serve as upper boundary conditions on the ocean model.

In a typical computational cycle, the atmospheric model is numerically integrated over a short time period Δt_1, with T^* held fixed. In the second part of the computational cycle, the ocean model is numerically integrated over a period Δt_2, with Q^*, $(E-P)^*$, and τ^* held fixed. The time periods Δt_1 and Δt_2 should be very short, compared to the adjustment time of the atmospheric and ocean models. For a one-to-one correspondence in time between the ocean and atmosphere, Δt_1 and Δt_2 should be exactly equal. Setting Δt_1 and Δt_2 equal to each other is not an efficient method for computing a climatic equilibrium, however, for two reasons. First, nearly an order of magnitude more computing is required to integrate the atmospheric model over the same period as the ocean model. This is due to the fact that high-speed external gravity waves are filtered out of the ocean model, but not out of the atmospheric model. Second, the atmospheric model is shown in part I to respond to external influences and reach a new equilibrium within a year or less, while

the ocean model with its much greater heat capacity would require centuries for a full adjustment. With these two factors in mind, Δt_2 is chosen to be 100 times longer than Δt_1 in each computation cycle of stage II. In the computational procedure, Δt_1 is chosen to be one-fourth of a day. To avoid an unrepresentatively large response by the ocean to transient disturbances in the atmosphere, the fields of Q^*, $(E-P)^*$, and τ^* are smoothed by taking a running mean over a period of several weeks. On each computational cycle, the running mean values of the flux of heat, water, and momentum are updated. This method of computation allows a feedback between the atmospheric and ocean model which seeks out a "climatic" equilibrium of mutual adjustment. In planning the numerical experiment it was felt that the merits of using an atmospheric model with a relatively complete treatment of the radiation balance and the general circulation outweighed the disadvantage of using time-smoothed boundary conditions for the ocean model.

It is possible to see the response of the average kinetic energy to the new boundary conditions (fig. 2). Within the first decade of stage II, the total kinetic energy has dropped to about 60 percent of its final value in stage I. For the remainder of the run, the kinetic energy level continues to oscillate in an irregular manner. The zonally averaged temperature curves shown in figure 3 indicate the large changes that take place in response to the new boundary conditions. At the 67-m level, an increase of temperature is indicated at all latitudes. The general warming at the surface is interpreted in part II (Manabe, 1969*b*) as the response of the joint system to the northward heat transport by ocean currents. The heat balance is altered in a dramatic way by the ocean currents, with the most important changes taking place in the northern part of the basin. South of 40° latitude, the zonally averaged temperature at the surface reaches a nearly steady value after the first two decades of stage II, while the surface temperature continues to climb slowly at higher latitudes.

At the 1-km level, the north-south gradient of temperature reverses during stage II. This feature shows up very clearly in figure 3c. This change brings the temperature structure of the model into much greater agreement with observations. A generally persistent warming trend[2] is shown in figures 3c and 3d, both at the 1-km and the 3-km level. The one-century (ocean time) duration of the run is evidently not nearly long enough to allow the deep water to come into equilibrium with the new boundary conditions. During stage II, the average temperature change per unit volume is 2° per century. To determine the flux of heat through the surface required to maintain this temperature change, we must multiply by the total depth.

$$\rho_0 c_p 2^\circ \times 4 \times 10^5 = 8 \times 10^5 \text{cal/cm}^2\text{/century}$$

or

$$1.5 \times 10^{-2} \text{ly/min.}$$

This net heating rate must be compared to the normal amplitude of the heat exchange between the ocean and atmosphere. It is shown by Manabe (1969*b*) in part II that the surface heating ranges from 0.1 to 0.2 ly min^{-1}. Thus the normal differences in surface heating from one part of the ocean to another are about one order of magnitude greater than the net heating required to heat up the abyssal water.

In table 2 of subsection 9B in part II (Manabe, 1969*b*), the net heating of the ocean is given as 1.0×10^{-2} ly min^{-1} or 30 percent less than the value given above. The difference is due to the fact that the larger value is based on an average over the entire period of stage II, while Manabe's value is based on only the final 30 yr of stage II.

7. RESULTS OBTAINED AT THE END OF STAGE II

This section is devoted to a description of the fields of temperature, salinity, and velocity obtained by first averaging with respect to time over the final 30 yr of stage II, and then averaging the two hemispheres together. In analyzing various features of the solutions, frequent reference will be made to the surface boundary conditions. The average fields of Q^*, $(E-P)^*$, and τ^* for the 30-yr period at the end of stage II are shown in figure 6. Various aspects of these fields have already been discussed from a meteorological standpoint in part II (Manabe, 1969*b*). The reader is referred to part II for a comparison of these fields with estimates for the real ocean given by Budyko (1958). The $(E-P)^*$ chart shown in figure 6 is modified along the ocean boundaries by the addition of runoff from the land. All runoff is assigned to the first row of points immediately adjacent to the boundary. As explained in part II, the runoff from the eastern half of the continent enters the ocean along the east coast of the continent, and the runoff from the western half goes to the west coast. All the Arctic runoff, in water and ice form, is evenly distributed along the north boundary of the ocean model.

The pattern of wind stress shown in figure 6 is the actual boundary condition for the ocean model during the final 30-yr period of stage II. During the analysis of the results, it was discovered that an error had been made in the communication subprogram, so that all the wind stresses generated by the atmospheric model were erroneously multiplied by $\cos\phi$. The ocean model computation is consistent internally, but the applied stresses are systematically too low at higher latitudes to correspond with the climate of the joint model. The effects of this inconsistency on the model climate are investigated in a special computation extending the integration of stage II over an additional 30-yr period. The results of this test computation are discussed in the appendix.

Figure 6c shows that a very vigorous cyclonic wind gyre is present in the subarctic region of the ocean in spite of

[2] An exception to the warming trend in figure 3d occurs at 57° and 63° latitude. Note that unrealistically low temperatures (less than −2°C) form at the 3-km level. This cooling, which is exactly compensated by a heating at the 1-km level, is a truncation error associated with the use of centered differences in calculating the vertical advection of temperature and insufficient resolution.

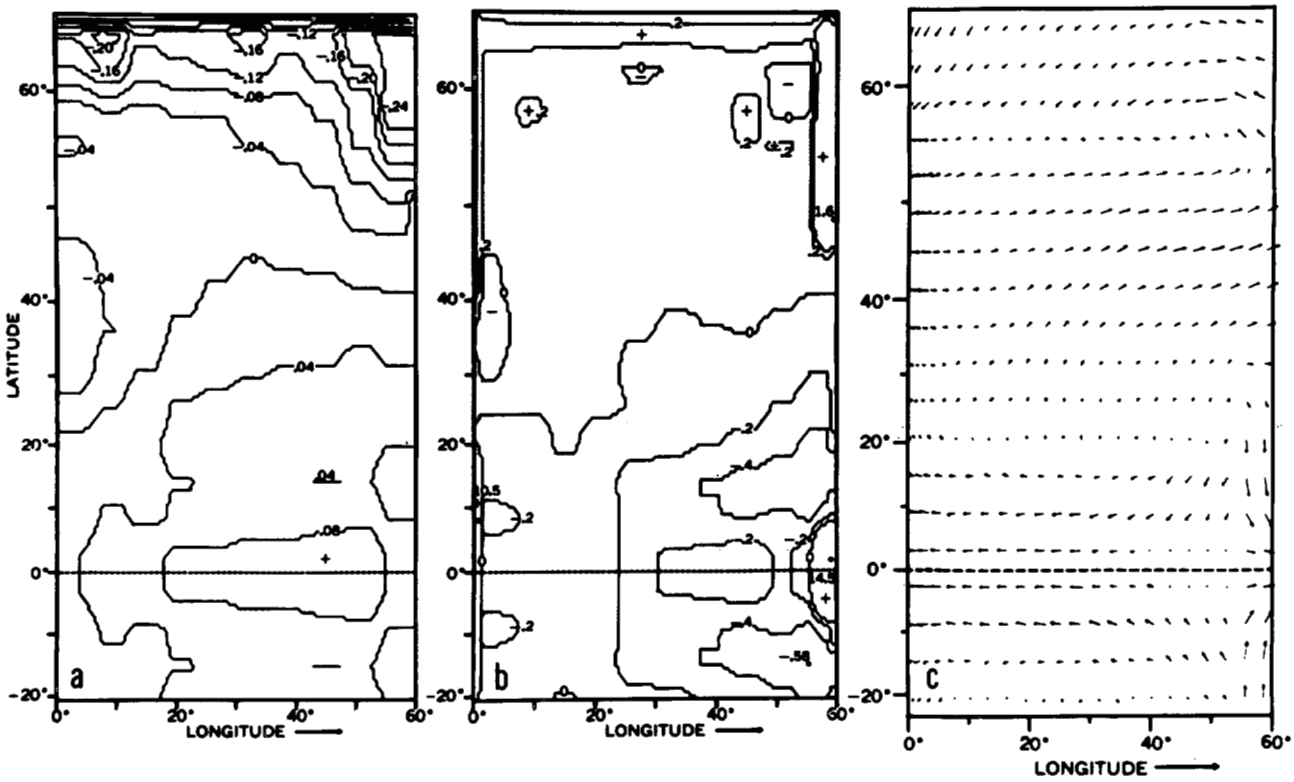

FIGURE 6.—Boundary conditions for the ocean model averaged over the final 30 yr of stage II. (a) the surface heat flux in ly min^{-1}, (b) the surface water flux in cm day^{-1}, and (c) the surface wind stress pattern. An arrow with a length of 2° of longitude represents a stress of 1 dyne cm^{-2}.

the bias toward lower stress values caused by the erroneous $\cos\phi$ factor. This vigorous pattern is associated with the extensive snow cover over land at high latitudes. The effect of a steady insolation without seasonal fluctuations in producing an early ice-age climate in the model is discussed in part II (Manabe, 1969*b*).

The average surface patterns of temperature, salinity, and surface drift are shown in figure 7a–d. Upwelling at the base of the surface mixed layer is shown in figure 7e. It is convenient to discuss the velocity patterns first. The most prominent features of figures 7c and 7d are the model analogs of the Gulf Stream and the Labrador Current which appear along the western boundary. The peak velocity is reached at a latitude of 20°. It is only 32 cm sec^{-1}—much less than what is actually observed (Stommel, 1965). The discrepancy is probably related to the level of lateral mixing and the numerical treatment. Even though the grid is carefully refined at the western boundary, the resolution is probably still too coarse and the level of lateral viscosity too high to get a western boundary current as narrow and intense as observed. The southward-flowing current along the western boundary in the subarctic reaches a speed of only 6 cm sec^{-1}. Examination of lower levels (not shown) indicates that it is an extremely deep current, however. The total transport of this current is comparable to the northward-flowing current to the south. The strong outflow in the surface layer from the Equator is directly associated with Ekman drift. Associated with this outflow is a strong band of upwelling of more than 10 cm day^{-1} along the Equator shown in figure 7e. Due to the coarse resolution in the north-south direction of the numerical net (fig. 1), this region is somewhat broader than the corresponding feature in the real ocean. Other regions of strong upwelling that play an important role in the surface heat balance are shown in figure 7e. One region is present along the east coast at low latitudes, and another is present along the west coast in middle and high latitudes. The upwelling in these boundary regions ranges from 10 to 100 cm day^{-1}. Note that the broad regions of downwelling in the subtropics and upwelling in the subarctic involve vertical motions at least one order of magnitude less. On the whole, the upward motion agrees quite closely with vertical velocity patterns obtained previously by Bryan and Cox (1967) for an ocean model with much more idealized surface boundary conditions.

One of the most striking features of both the observed and computed patterns of surface salinity and temperature is the tendency for isotherms and isohalines to be concentrated on the western side of the ocean in middle latitudes and spread out on the eastern side of the ocean. This feature appears to be closely related to the pattern of upwelling and currents. The fact that the isohalines are more concentrated than the isotherms may be explained

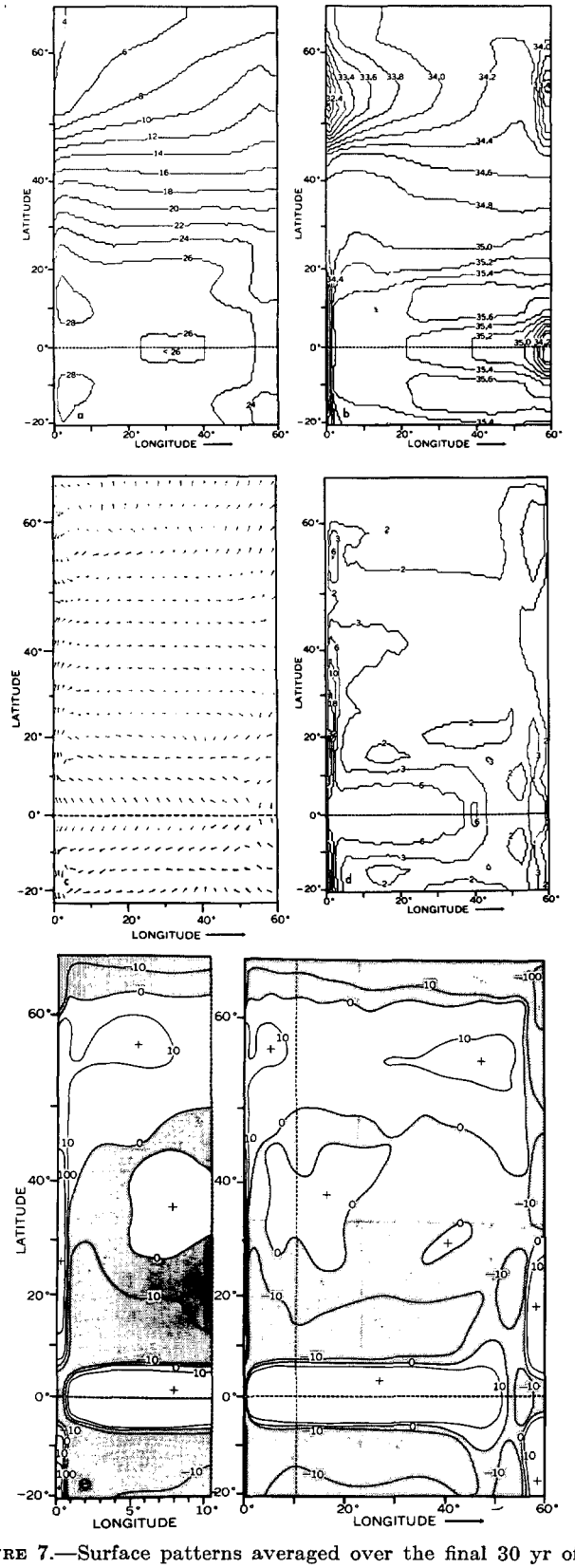

FIGURE 7.—Surface patterns averaged over the final 30 yr of the run. (a) surface temperature in degrees Celsius; (b) surface salinity °/₀₀; (c) direction of surface currents; (d) velocity isotachs in cm sec^{-1}; and (e) upwelling at the base of the surface layer given in cm day^{-1} (right, the whole basin, and left, an expanded diagram to show detail near the western boundary).

by several factors. Probably the most important is a negative feedback mechanism in the surface heat balance that tends to suppress temperature anomalies with respect to the zonal average. A similar mechanism does not exist for salinity.

Another factor is that salinity may act much more like a tracer than temperature, because it has a much smaller effect on the density field in lower and middle latitudes. Through the geostrophic relation, the isotherms are very nearly streamlines of the vertical shear of the current, and hence of the current itself in many areas. To the extent that isotherms and streamlines of the flow coincide, the advection will be weak. Salinity, on the other hand, is much more weakly correlated with density, and the advective effects can be that much stronger.

Very little runoff occurs in low temperate latitudes in the model. In the region from 50° to 60° latitude, it is interesting to note in the computed salinity pattern of figure 7b that the salinity minimum on the western boundary is displaced southward relative to the salinity minimum on the eastern boundary. A much larger difference in the latitude of the salinity minima on the east and west sides of the ocean is present in the observed pattern. The salinity minimum in the Grand Banks Region is about 10° south of the salinity minimum in the North Sea Region. Aside from differences in the precipitation pattern on the two sides of the ocean, the strong boundary current flow must be important in causing the minimum on the western side to be displaced southward.

Much less favorable agreement between observation and the present computations exists in the position of the salinity maximum. The observed pattern in figure 8 shows the salinity maximum displaced 20° to 25° of latitude away from the Equator, while in the computed pattern the salinity maximum is centered at a latitude of 10°. An examination of figure 7b indicates that the computed salinity maximum coincides closely with the computed field of vertical water flux. The southward shift of the salinity maximum is evidently associated with a general southward displacement of the climatic zones in the atmosphere-ocean model. This feature is discussed more fully in part II (Manabe, 1969*b*).

From a quantitative standpoint, the absolute value of the salinity is about 1.4 parts °/₀₀ less than observed in the North Atlantic. The relative difference between the average salinity at 60° latitude in the central part of the ocean and the salinity maximum is about 2 °/₀₀ in the North Atlantic, but only 1.6 °/₀₀ in the model.

In figure 9, the patterns of temperature and salinity are given for the 300-m level. In general, the patterns of the isotherms and the isohalines are very similar. One exception occurs at the eastern boundary at high latitudes. The isotherms have a northeast-southwest tilt, while the isohalines are tilted the opposite way so that a slight minimum occurs at the eastern wall. The surface drift pattern in figure 7c indicates that strong downwelling takes place along the eastern wall at high latitudes. Downwelling produces a warming at the 300-m level. Precipitation and runoff are so intense in this area, however, that a halocline forms, reversing the usual ver-

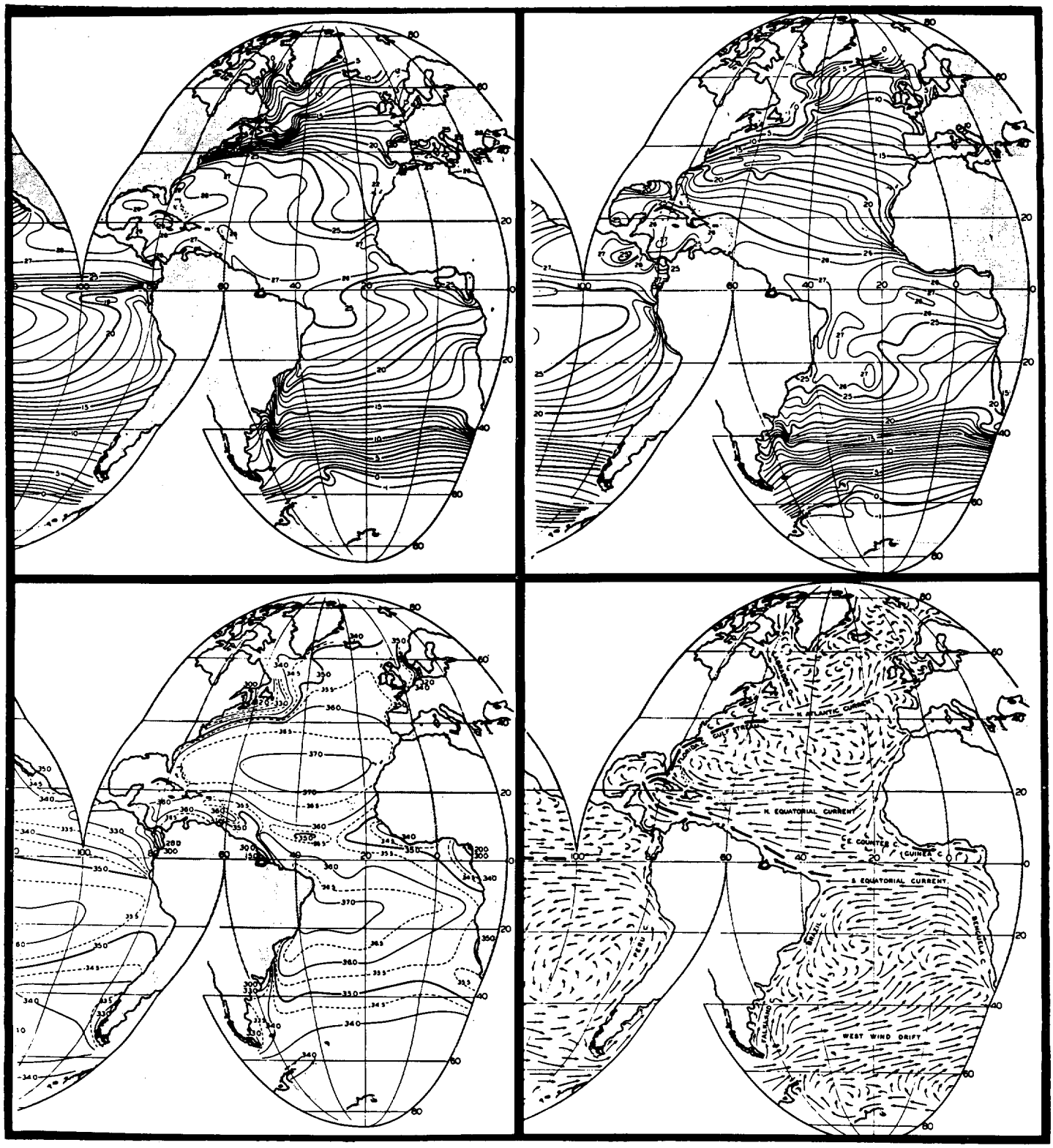

FIGURE 8.—Observed surface patterns for the Atlantic (Sverdrup and others, 1942). Upper left, temperature in July; upper right, temperature in January; lower left, salinity; and lower right, surface drift.

tical gradient of salinity. Thus downwelling acts to freshen the water at the 300-km level, rather than increasing the salinity.

The observed temperature patterns at the 200- and 400-m level are shown in figure 10. Generally, the observed temperature gradients at this level are much stronger than the calculated gradient due to the rather coarse grid and large lateral mixing of the model. The temperature patterns observed and calculated are roughly similar at high latitudes except for the minimum value. The minimum

value calculated is about 4°, while the observed minimum is about 0°C. At low latitudes the calculated temperature at 300 m is over 16°C. The observed temperature even at 200 m near the Equator ranges from 12° to 14°. Observation thus indicates a much shallower thermocline in the vicinity of the Equator than the ocean model.

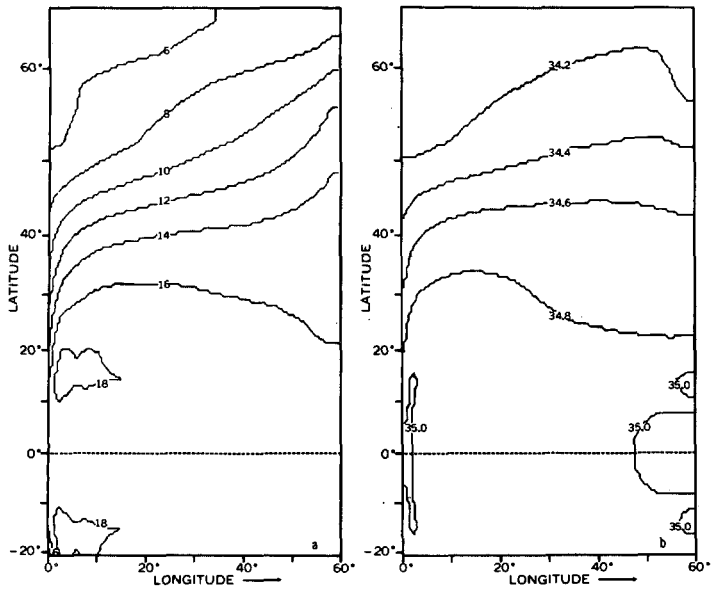

FIGURE 9.—Fields of temperature (left) and salinity (right) at a depth of 300 m for the model.

Zonally averaged temperature and salinity sections in a north-south vertical plane are shown in figure 11. The figure allows a comparison of the initial state of stage I to the final 30-yr average of stage II. The temperature pattern shows very clearly the large mass of very cold water trapped in the bottom of the basin without an outcrop at the surface. As mentioned in the previous section, the very cold deep water is a relic of the initial conditions and stage I. During stage II the bottom is gradually warming up at the rate of approximately 2° per century, but a much more extensive numerical integration would be required to bring the entire abyssal water mass into equilibrium. The salinity pattern in figure 11 has many of the features of the South Atlantic in the observed section in figure 12. A salinity maximum is present near the surface in the region between the Tropics and subtropics, coinciding with the region of maximum $(E-P)^*$. A halocline is also present in the polar zone similar to that found around the Antarctic Continent. One of the most interesting features is a layer of intermediate water characterized by a pronounced salinity minimum at 1000 m. The tongue of intermediate water shown in figure 12 is the Antarctic intermediate water, but a similar feature is found in the North and South Pacific as well.

As mentioned previously in connection with figures 9 and 10, a very evident failure of the numerical model is

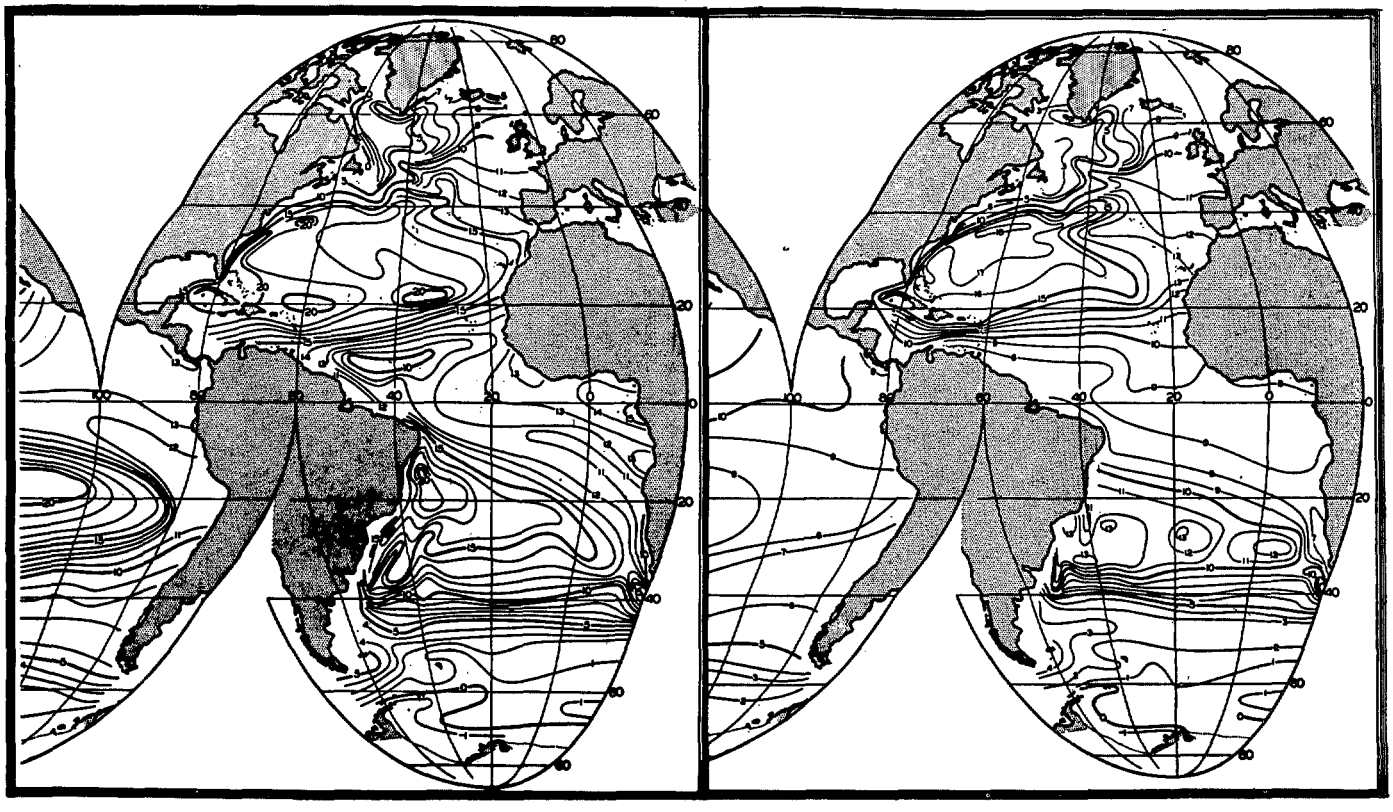

FIGURE 10.—Fields of temperature for 200 m (left) and 400 m (right) from Sverdrup and others (1942).

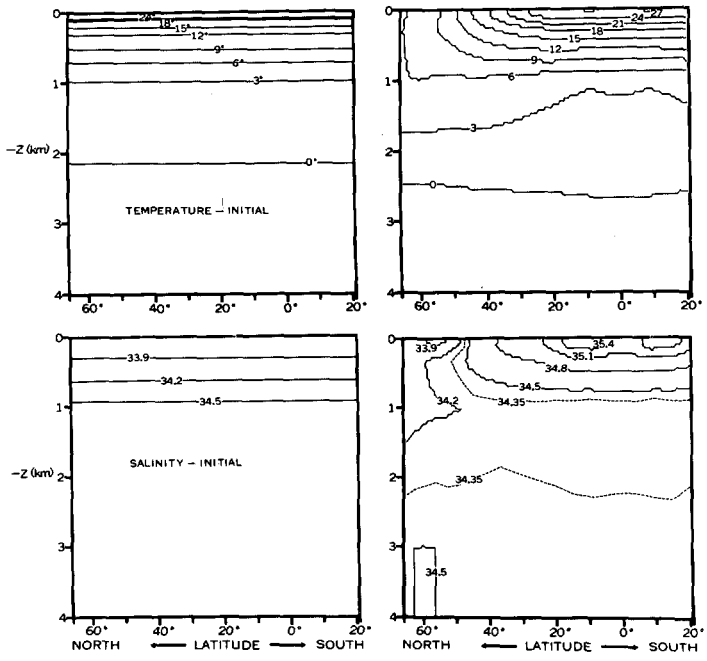

FIGURE 11.—Vertical cross-sections of the zonally averaged fields of temperature (upper) and salinity (lower). Final patterns are shown on the left.

connected with the thickness of the thermocline at the Equator. Both the salinity and temperature cross-sections in figure 11 indicate a thermocline near the Equator which is many times deeper than that observed. It is not clear whether this feature is due to the large lateral mixing of heat and salinity in the model, or due to the omission of some important effects of the stratification on vertical mixing. Additional carefully planned numerical experiments with more detailed resolution are required to understand this deficiency of the model.

8. THE THERMOHALINE CIRCULATION AND THE MERIDIONAL TRANSPORT OF HEAT AND SALINITY

Due to the existence of a large isolated reservoir of cold water in the lower part of the basin, the thermohaline circulation is for the most part confined to the upper 2 km. Integrating the continuity equation with respect to λ, we obtain

$$\int_0^{\Delta\lambda} \cos\phi w_z d\lambda + \int_0^{\Delta\lambda} (\cos\phi v)_\phi d\lambda = 0 \qquad (30)$$

where $\Delta\lambda$ is the width of the ocean basin. From this

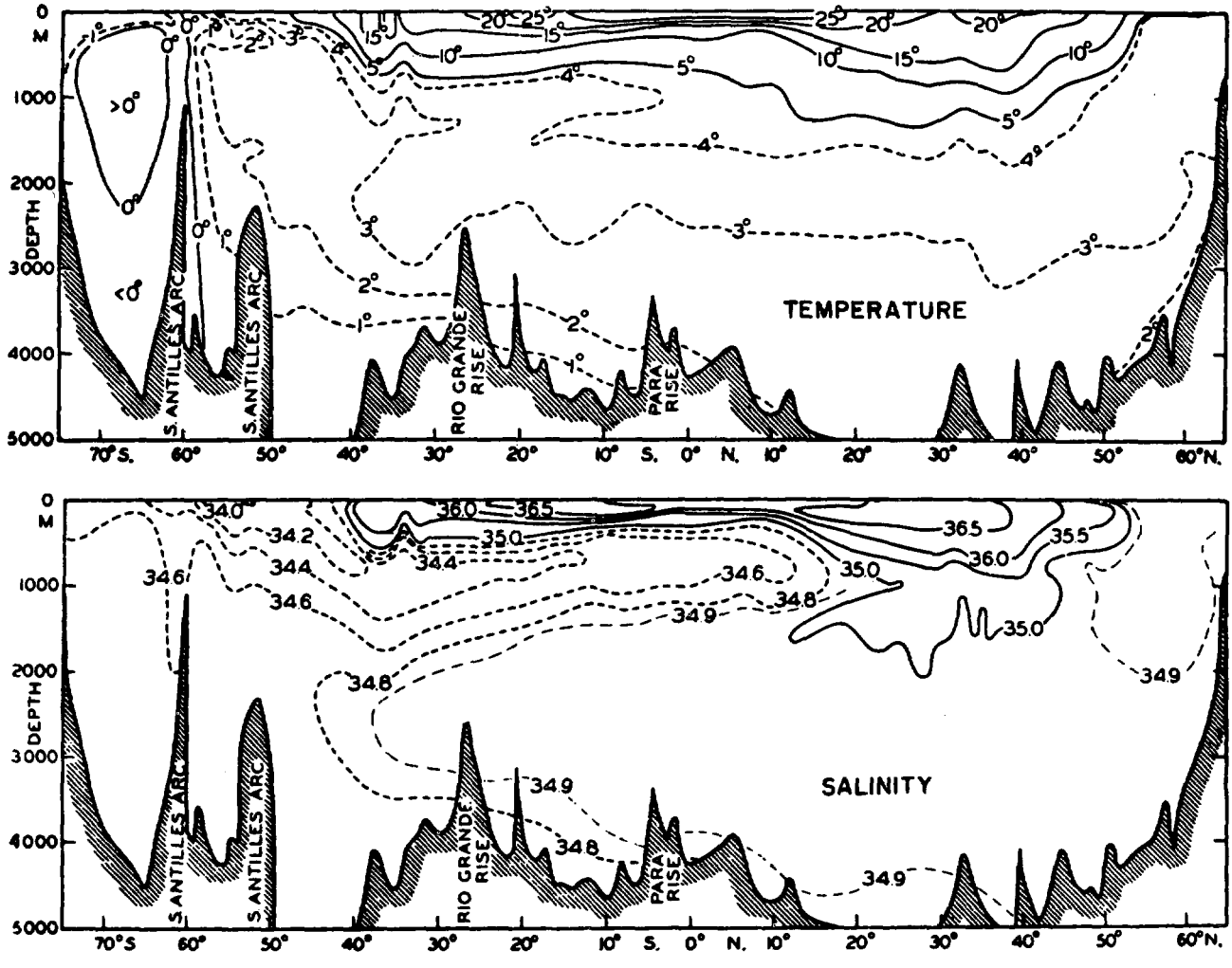

FIGURE 12.—Vertical sections of temperature (upper) and salinity (lower) of the Atlantic (Sverdrup and others, 1942).

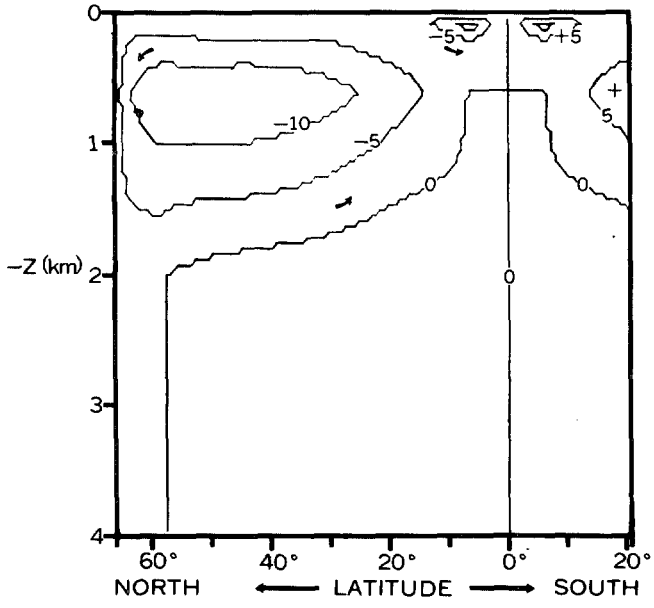

FIGURE 13.—Pattern of mass transport of the meridional circulation in units of 10^6 metric tons sec^{-1}.

relationship it is possible to specify the zonally averaged meridional circulation in terms of a transport stream function.

$$\cos\phi\int_0^{\Delta\lambda}\rho_0 v\,d\lambda=-\psi_\phi \tag{31}$$

and

$$\cos\phi\int_0^{\Delta\lambda}\rho_0 v\,d\lambda=\psi_z. \tag{32}$$

The pattern corresponding to the thermohaline circulation is shown in figure 13.

A general rising motion prevails at lower latitudes, and a much more confined region of sinking is present near the north wall. A small independent counterclockwise gyre exists near the surface in the Tropics. The general pattern is similar to the meridional flow obtained by Bryan and Cox (1967). Bryan and Cox's calculations show that the secondary shallow overturning circulation in the Tropics is not really part of the thermohaline circulation, but primarily due to the wind. The upper branch of this gyre consists of poleward Ekman transport in the trade wind region. A striking feature of the pattern shown in figure 13 is the limited penetration of the downward branch of the circulation near the north wall. This feature is associated with the large isolated mass of dense cold water in the bottom of the basin, a relic of stage I.

The strength of the circulation given in figure 13 is 10 Sverdrups (10^{13} gm sec^{-1}). The total mass of water in the northern or the southern half of the basin is 8.4×10^{22} gm. To obtain an idea of the "turnover" time or "flushing" time of the circulation, one must divide the total mass of water by the mass transport of the thermohaline circulation. The result is 461 yr. If only the active part of the basin above 2 km is considered, the turnover time is reduced to only 230 yr. Evidence based on measurements of C_{14} in the Atlantic indicate an age of 8 to 10 centuries for the deep water. However, there is reason to believe that much of the Atlantic deep water is bypassed by the main thermohaline circulation, so the age of the deep water determined by C_{14} gives an overestimate of the average turnover time. Some indications of this are shown in the salinity section for the Atlantic shown in figure 12. The salinity pattern appears to indicate that the upwelling at the base of the thermocline over large areas is sustained by the Antarctic intermediate water rather than by Atlantic deep water.

The expression for total meridional heat transport may be written,

$$H_4=c_p\rho_0\{vT+A_H T_\phi a\}$$

where { } denotes an integral over an entire latitudinal wall across the basin. Let [ ] denote a zonal average, and a prime the departure from a zonal average. Using this notation, it is possible to isolate the contribution of the meridional circulation

$$H_4=H_1+H_2+H_3 \tag{33}$$

where

$$H_1=c_p\rho_0\{[v][T]\},$$

$$H_2=c_p\rho_0\{[v'T']\},$$

and

$$H_3=c_p\rho_0 A_H\{[T]_\phi\}/a. \tag{34}$$

The term H_1 may be interpreted as the heat transport associated with the meridional circulation shown in figure 13. The second term, H_2, is the contribution of correlations between departures from zonal averages. It may be thought of as the component associated with horizontal gyres. The final term, H_3, is the contribution of lateral mixing to the total poleward heat transport. The dependence of all of the three components on latitude is shown in figure 14a.

The most obvious feature of figure 14a is that H_3 is relatively insignificant. The most important contribution is H_1, the thermohaline component. The magnitude of this term can be roughly estimated in advance as the product of the total transport of the thermohaline circulation times the temperature difference between the upper and lower branches. Note that the poleward heat transport decreases rapidly in the subarctic zone. Since the strength of the thermohaline circulation is nearly constant in this zone, this is almost entirely due to the decreasing temperature difference between the upper and lower branches of the thermohaline circulation.

An intuitive view of heat transport by ocean currents in the North Atlantic is that the Gulf Stream carries heat northward and that the northward flow is compensated by the return of colder water on the eastern side of the

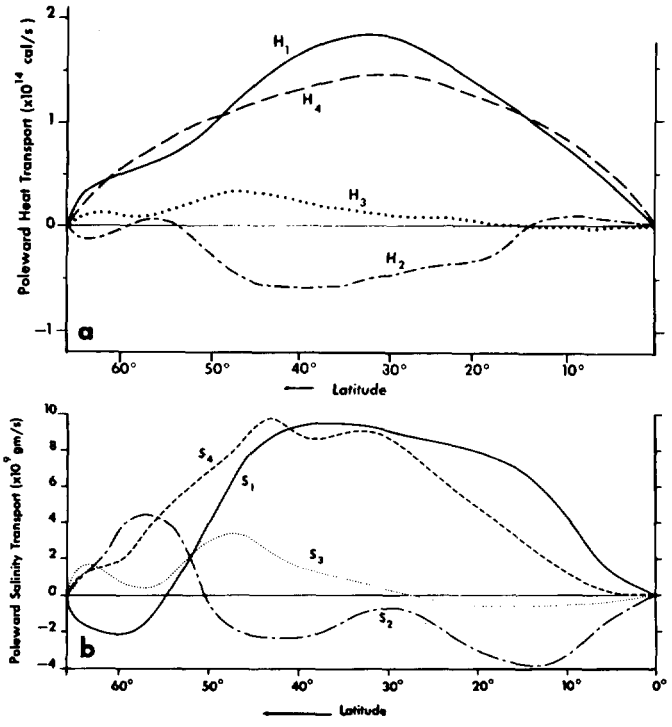

FIGURE 14.—(a) components of the poleward heat transport and (b) components of poleward salinity transport.

ocean. In the model, a very different regime exists. The horizontal gyre component H_2 actually transports heat toward the Equator. The equatorward flow on the eastern side of the ocean is actually warmer than the poleward flow on the western side. Poleward heat transport is accomplished by the fact that much of the poleward flow along the western boundary is part of the meridional circulation and from the standpoint of continuity is compensated by a return flow at lower levels.

Observations are not detailed enough to make similar calculations for the Atlantic and Pacific with very much confidence. Geostrophic calculations by the author (Bryan, 1962) based on Meteor and IGY hydrographic data tend to support the idea that the H_1 term dominates the heat transport. On the other hand, the same observational study (Bryan, 1962) showed that H_2 was positive at 30° N. in the North Atlantic and about 50 percent of the value of H_1. The observational results for H_2 and the results based on the model are, therefore, not in agreement. Further research is needed to resolve this point, which is of considerable importance in the large-scale heat balance of the ocean.

As far as the net overall value of the poleward heat transport is concerned, it is possible to compare it with several studies of the heat balance of the ocean surface. Estimates of poleward heat transport, obtained through an area integration with respect to latitude of the surface heat balance, are shown in figure 15. An important feature of the Atlantic is a considerable heat transport across the Equator, caused by a net drift of surface water

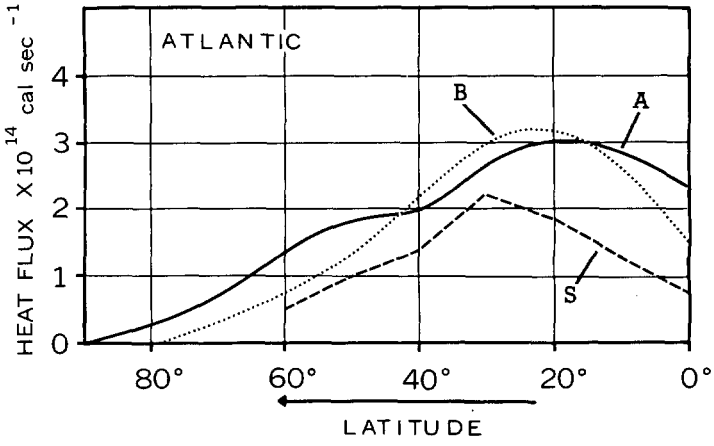

FIGURE 15.—Estimates of poleward heat transport based on surface heat balance calculations (Bryan, 1962). The curves A, B, and S correspond to the heat balance calculations of Albrecht (1960), Budyko (1958), and Sverdrup (1957), respectively.

from the South Atlantic into the North Atlantic (Sverdrup, 1957). Subtracting a portion of the heat transport to correct for this feature, the heat balance studies indicate a value of $1.0-1.5\times10^{14}$ cal sec^{-1}. This corresponds very closely with the model results shown in figure 14a. As pointed out in a more detailed discussion in Bryan and Cox (1967), the level of heat transport is largely determined by the magnitude of vertical mixing. The vertical mixing coefficient κ determines the rate at which heat is taken up by the ocean at low latitudes and, therefore, the strength of the thermohaline circulation. Although the temperature structure is still changing in deep water, the choice of 1.5 cm^2 sec^{-1} for κ in this numerical experiment not only gives a representative thickness of the thermocline in middle latitudes but also a reasonable partitioning of the poleward heat transport between the ocean and the atmosphere. The major difficulty is the thickness of the thermocline near the Equator mentioned earlier, which probably indicates a constant κ may be inadequate for a detailed model of the ocean.

The physical meaning of salt transport in the model requires some additional explanation. The boundary conditions on the model require it to be a fixed volume of fluid with the normal component of velocity equal to zero at all boundaries. The salinity balance is, therefore, treated implicitly. An excess of rainfall over evaporation at the surface is considered a sink of salinity which is proportional to the local salinity as shown in section 5. Therefore, a net poleward transport of salt would be present in the model even in the case of a stationary salinity field. The expression for the total salinity transport is similar to that for heat transport given by equation (33),

$$S_4=S_1+S_2+S_3 \tag{35}$$

where

$$S_1=\{[v]\,[S]\},$$
$$S_2=\{[v'S']\},$$

and

$$S_3=A_H\{[S]_\phi\}/a. \tag{36}$$

The three components of salinity transport are shown in figure 14b. The main features of salinity transport are very similar to that of heat transport. This similarity is quite natural since the source and sink distribution for salinity and heat are arranged in much the same way. The major source area is the low precipitation region in the subtropics. The major sink is the area of high rainfall and low evaporation in the subarctic. An exception to the analogy exists at the Equator due to high runoff.

As in the case of heat transport, the major component is connected with the meridional circulation. In high latitudes, a halocline is present so that the vertical gradient of salinity is reversed. The meridional circulation shown in figure 13 consists of a northward flow at the surface and a return drift at low levels both in the subarctic and subtropics. As a result, the S_1 component reverses in sign at the equatorward edge of the halocline. The effect on the total transport is compensated by the subarctic gyre indicated in the S_2 component. In the subarctic, the intense southward-moving current along the western boundary is correlated with low salinity, and the northward drift in the eastern part of the gyre with relatively high salinity.

As mentioned earlier, the transport of salinity in the model implies a net movement of fresh water through the ocean in the opposite direction. Thus a poleward transport of salinity implies a net equatorward flow of water in the ocean. Such a flow is required to maintain a steady state in the presence of poleward transport of water vapor by the atmosphere. In the more general case, there is also a component of poleward water transport by rivers to be taken into account, but the simplified treatment of runoff in the present climate model eliminates this effect. Unfortunately, no observational studies are available on the way in which salinity is actually transported by ocean currents for comparison with figure 14b. Data studies of this type should be attempted, as they would yield important information on the global hydrological cycle that could be obtained in no other way.

9. THE ENERGY BUDGET

In the study of the atmosphere, a comparison of the energy budget computed from observations with the results of numerical models has contributed a great deal to the present understanding of large-scale motions. Unfortunately, similar observational material is not available for the World Ocean, but it may still be fruitful to examine the main features of energy budget of the present ocean model. The energy budget gives an insight into the physics of ocean circulation which cannot be obtained by simply examining fields of temperature, salinity, and velocity.

If the equation for the horizontal components of motion is multiplied by $\rho_0\mathbf{v}$, we obtain

$$\rho_0(\mathbf{v}^2/2)_t=-\rho_0\mathbf{v}[\mathbf{v}\nabla\mathbf{v}+w\mathbf{v}_z] -\mathbf{v}\nabla p+\rho_0\mathbf{v}\kappa(\mathbf{v})_{zz} +A_M\rho_0\mathbf{v}\mathbf{F}. \quad (37)$$

TABLE 3.—*Energy budget per unit area of the ocean surface for the final 30 yr of stage II. Units are ergs cm^{-2} sec^{-1}.*

Buoyancy term	$-\langle g\rho w\rangle H$	−0.31
Vertical friction (primarily work done by wind)	$\langle\kappa\rho_0\mathbf{v}\mathbf{v}_{zz}\rangle H$	.92
Lateral friction	$\langle\rho_0 A_M\mathbf{v}\mathbf{F}\rangle H$	−.61

Here, $\langle\ \rangle$ will denote an average taken over the entire volume of the model ocean. Using the continuity and hydrostatic relations given by equations (2) and (3) respectively, the volume average of the second term on the right-hand side of equation (37) may be written,

$$\langle\mathbf{v}\nabla p\rangle=\langle pw_z\rangle=\langle g\rho w\rangle. \quad (38)$$

Taking the volume average of both sides of equation (37), we obtain

$$\langle\rho_0\mathbf{v}^2/2\rangle_t=-\langle g\rho w\rangle+\kappa\langle\mathbf{v}\rho_0\mathbf{v}_{zz}\rangle+\langle A_M\rho_0\mathbf{v}\mathbf{F}\rangle. \quad (39)$$

The term on the left is the change of the kinetic energy per unit volume, consistent with the approximations of the present model. The first term on the right represents the work done by buoyancy forces. This term is the link between the potential energy and kinetic energy. A negative correlation between density and vertical motion leads to a lowering of the center of gravity of the system and a corresponding increase of kinetic energy.

The second term on the right is the dissipation due to the vertical mixing of the momentum. For the present calculation, the first layer contributes over 95 percent of this term, and so it primarily represents the work done by surface wind stress. The third term on the right-hand side is the dissipation due to lateral friction.

The contribution of the three terms on the left-hand side of equation (39) to the energy cycle is shown in table 3. The volume averages are multiplied by the depth to give the work done per unit horizontal area. The dominant term is the work done by wind, which is 0.92 ergs cm^{-2} sec^{-1}. This term is compensated by lateral friction and work done by buoyancy forces.

10. CONCLUSIONS

In one sense, the numerical experiment is a failure in that the original goal of calculating a climatic equilibrium with the joint system is not attained. Due to the choice of initial conditions, the time period required to bring the enormous reservoir of abyssal water in the ocean equilibrium is exceedingly large. The numerical integration is terminated at a stage when the atmosphere has settled down to a nearly steady state and the deep water is heating up at a slow, but nearly constant rate. A nearly constant net flux of heat is directed from the atmosphere down into the ocean. This flux amounts to 1.5×10^{-2} ly min^{-1} or a little less than 1 percent of the solar constant. The average heating rate per unit volume of the ocean is 2° per century. Many features of the final solution are quite close to observed data for the real ocean, even though the system is still in a transient state. It is not clear, however, what the final solution will be when the ocean has heated up sufficiently and a true equilibrium is reached.

A balance between ice growth, advection of ice by ocean currents, and melting in warmer ocean areas exists in the Arctic areas in the first stage of the ocean calculation. While the ice model is highly simplified, the solutions give a very realistic mean ice thickness of 3 to 5 m. In the second stage of the calculation, the interaction between the ocean and atmosphere system permits the surface temperatures to rise above freezing in the northern part of the basin. After a short time, the ice pack disappears and ceases to be a factor in the climate of the model.

The numerical experiment shows in a very clear way the effect of the transport of heat by ocean currents in the global heat balance. This effect is documented in detail in part II (Manabe, 1969*b*). As shown by Stommel and Webster (1962), the intensity of the deep ocean circulation is critically dependent on the vertical mixing coefficient, κ. Since a rather close agreement is obtained in the level of poleward heat transport of the model with estimates for the real ocean based on the work of Budyko (1958) and others, the choice of κ equal to 1.5 cm^2 sec^{-1} appears to have been a fortunate one. A whole series of numerical experiments would be needed, however, to determine just how critical this choice is. An apparent discrepancy does exist in the vertical structure of the thermocline, which also depends on the vertical mixing. In the tropical areas of the model mean, the thermocline is much deeper than indicated by observation. This difficulty forms an important problem for future investigation.

A detailed breakdown of the different components of poleward heat transport indicates that overturning in the vertical meridional plane is the most important component at low and middle latitudes. The subarctic gyre plays an important role at high latitudes in transferring heat. Poleward heat transport by horizontal mixing is relatively unimportant, indicating that the particular choice of the horizontal mixing coefficient is not a significant factor in the large-scale heat balance.

Compared with previous computations of ocean circulation, the surface boundary conditions of the present study are unique in the freedom with which the surface temperature and salinity structure is allowed to adjust itself. While the fixed boundary conditions used by Bryan and Cox (1967, 1968*a*, *b*) greatly simplifies the analysis, it produced many artificial features in the surface patterns. The surface temperature distribution of the present model has many features in common with that of the North Atlantic. The coldest water is found in the subarctic along the western boundary. Concentrated surface gradients are formed near the western boundary, but the isotherms produce a pronounced cold spot that appears to have a profound influence on the tropical precipitation pattern.

The salinity field is horizontally uniform initially, but during the course of the run it is transformed into a highly realistic pattern. A "halocline" forms at high latitudes, and a surface maximum appears in the subtropics. The north-south salinity gradient is very close to that observed in the North Atlantic and North Pacific. Although the numerical grid can just barely resolve it, a distinct body of intermediate water is found at the base of the "thermocline." This intermediate water outcrops at the surface in the subarctic gyre and is very similar to the Antarctic intermediate water of the Southern Hemisphere oceans.

The numerical experiment is somewhat marred by an error in the wind stress boundary condition over the ocean. The wind stress applied to the ocean is systematically too small by a factor of $\cos\phi$. The effect of this error is investigated by making a 30-yr extension of the numerical integration. From the results of this run, it is found that the interior drift is much stronger. This drift is poleward in subarctic latitudes and equatorward at subtropical latitudes. The interior surface drift is associated with relatively warm surface water compared to the boundary currents of the numerical model. The result is a strengthening of poleward heat transport at high latitudes and a decrease in poleward heat transport at low latitudes. A corresponding change takes place in the salinity transport. Most of this change in transport is associated with a slow change in the temperature structure of the ocean, so that the vertical heat exchange with the atmosphere remains nearly the same as in the main run.

The experience gained in this study should be valuable in designing future numerical experiments in climate. The failure to reach an equilibrium after very lengthy computations indicates that the straightforward integration of an initial value problem is not a practical method in dealing with an ocean model. In the case of the atmospheric model, about 1 yr is required to reach equilibrium after some important change in boundary conditions. A time step of about 10 min is required for the atmospheric model. The ratio of time step to total relaxation time is therefore about $1:5\times10^4$. In the case of the ocean model, the time step may be an order of magnitude larger, but the relaxation time to respond to new boundary conditions is almost three orders of magnitude longer. As a result, the ratio of time step to relaxation time for the ocean model is much less favorable, $1:5\times10^6$. This difference suggests that new methods should be tried to push the ocean toward a climatic equilibrium in a more efficient manner. Several approaches such as repeated interpolation suggest themselves, but detailed tests must be carried out to select the most accurate and effective method. Once this has been accomplished, the way will be open for much more ambitious computations than the present one. Future studies should take into account the actual configuration of the earth's continents and ocean basins. Once confidence in the models to simulate the earth's present climate has been established, it may be possible to use the models to reconstruct the climate existing for different continent-ocean configurations existing in the geologic past.

APPENDIX—EXTENSION OF STAGE II WITH CORRECTED WIND STRESS VALUES

The purpose of this appendix is to describe a test to determine the effects of an error in the calculations de-

TABLE 4.—*Maximum strength of the circulation in the vertical meridional plane and in the major wind gyres given in units of 10^6 metric tons sec $^{-1}$*

	Stage II	Corrected run
Thermohaline circulation (vertical, meridional plane)	14.72	14.69
Subtropical gyre (horizontal plane)	15.21	18.40
Subarctic gyre (horizontal plane)	-43.71	-84.80

scribed in the main body of the paper. A 30-yr extension of stage II has been carried out in which this error is removed. Over the main run, the atmospheric and oceanic models are internally consistent, but the wind stress fields used as an upper boundary condition on the ocean and a lower boundary condition on the atmosphere differ by a factor of cos ϕ. Here, we confine ourselves to a discussion of the response of the ocean model in the corrected run. The effect of the correction on the "climate" of the atmospheric model is described by Manabe (1969*b*). Due to long-term transients in the thermal structure of the model, no firm conclusions can be drawn concerning the ultimate effect the error would have on a steady equilibrium, but the corrected run provides an interesting test of the response of the ocean model to a significant change in surface wind patterns.

It might be expected that the thermohaline circulation would not be affected by a change in surface winds. This is confirmed in table 4 which shows that the total circulation in the meridional plane changes by less than 1 percent, when the average over the final 30 yr of stage II is compared with the final decade of the corrected run. The horizontal transport gyres are naturally more sensitive to the surface stress. The zonal average of the λ-component of the stress for stage II is compared to an average over the final decade of the corrected run in figure 16. The differences between the two stress profiles are not as great as one would expect due to the cos ϕ factor alone. Due to our method of computing conditions, one decade of ocean time corresponds to only 5 weeks of atmospheric time. For this reason it is not certain how representative the wind stress profile is, but evidently some compensation has taken place so that the difference is less than one would expect on the basis of the cos ϕ factor alone.

If inertial effects in the vertically integrated form of the vorticity equation are neglected, the meridional transport can be calculated from the Sverdrup formula (Stommel, 1965),

$$\frac{2\Omega \cos\phi}{a}\int_{-H}^{0}\rho_0 v dz = \mathrm{curl}_z \boldsymbol{\tau}^s. \tag{40}$$

On the left is the beta term of the vorticity equation and on the right is the curl of the surface wind stress. If we assume that the gyres consist of a Sverdrup flow in the interior compensated by a narrow boundary current at the west coast, the total strength of the gyre may be estimated by integrating both sides of equation (40) with respect to λ,

$$\int_{\lambda_1}^{\lambda_2}\int_{-H}^{0}\rho_0 v dz \cos\phi\, d\lambda = \frac{a}{2\Omega\cos^2\phi}\int_{\lambda_1}^{\lambda_2}\left[\frac{\partial \tau^\phi}{\partial\lambda}-\frac{\partial}{\partial\phi}\cos\phi\tau^\lambda\right]\cos\phi\, d\lambda. \tag{41}$$

The left-hand side of equation (41), computed from the wind stress patterns, is shown in figure 16b. The curl of the wind stress is generally more intense in the corrected run. In addition, the region of positive wind curl extends from latitude 40° all the way to the poleward boundary in the corrected run, while the region of positive wind curl is much more restricted in the main run. Qualitatively, the Sverdrup theory explains the intensification of the wind gyres shown in table 4.

Although the intensity of the overall meridional circulation remains nearly the same, important changes take place in the vertical structure of the thermohaline circulation near the surface. Through Ekman transport, the wind stress may either enhance or inhibit the upper branch of the thermohaline circulation. The net poleward transport in the upper layer is shown in figure 17. This layer is 67 m thick, and the net transport in this layer is particularly significant in poleward heat transport. The transfer of warm surface water in this layer must be compensated by the return flow of much colder water at deeper levels. Note that at most latitudes the net poleward drift in the surface layer is less in the corrected run than it is in the main run. The largest poleward transport in the surface layer takes place in the Tropics where the wind stress and thermal forces combine to cause a northward flow.

The effect of these changes in the circulation on the poleward transport of heat is indicated in table 5. The heat transport is broken down into the basic components defined in section 8. H_1, H_2, and H_3 are the components due to the meridional circulation, horizontal gyres, and lateral mixing, respectively. H_4 is the total poleward heat transport. From the change in total heat transport, it can be seen that the main effect of the change in wind is to increase heat transport at high latitudes and decrease it in lower latitudes. Little change takes place in middle latitudes. It is possible to see a close correspondence in the behavior of the H_1 component and the poleward mass transport in the upper layer shown in figure 17. The H_1 component is generally lower in the corrected run, except at very high latitudes. The poleward mass transport has the same behavior. In middle latitudes the decreased values of H_1 are compensated by an increase in H_2, the gyre component. The most significant changes in the total transport occur when H_1 and H_2 are of the same sign. This takes place at 61° near the poleward wall and at 17° latitude. In each case the transport changes by approximately 20 percent.

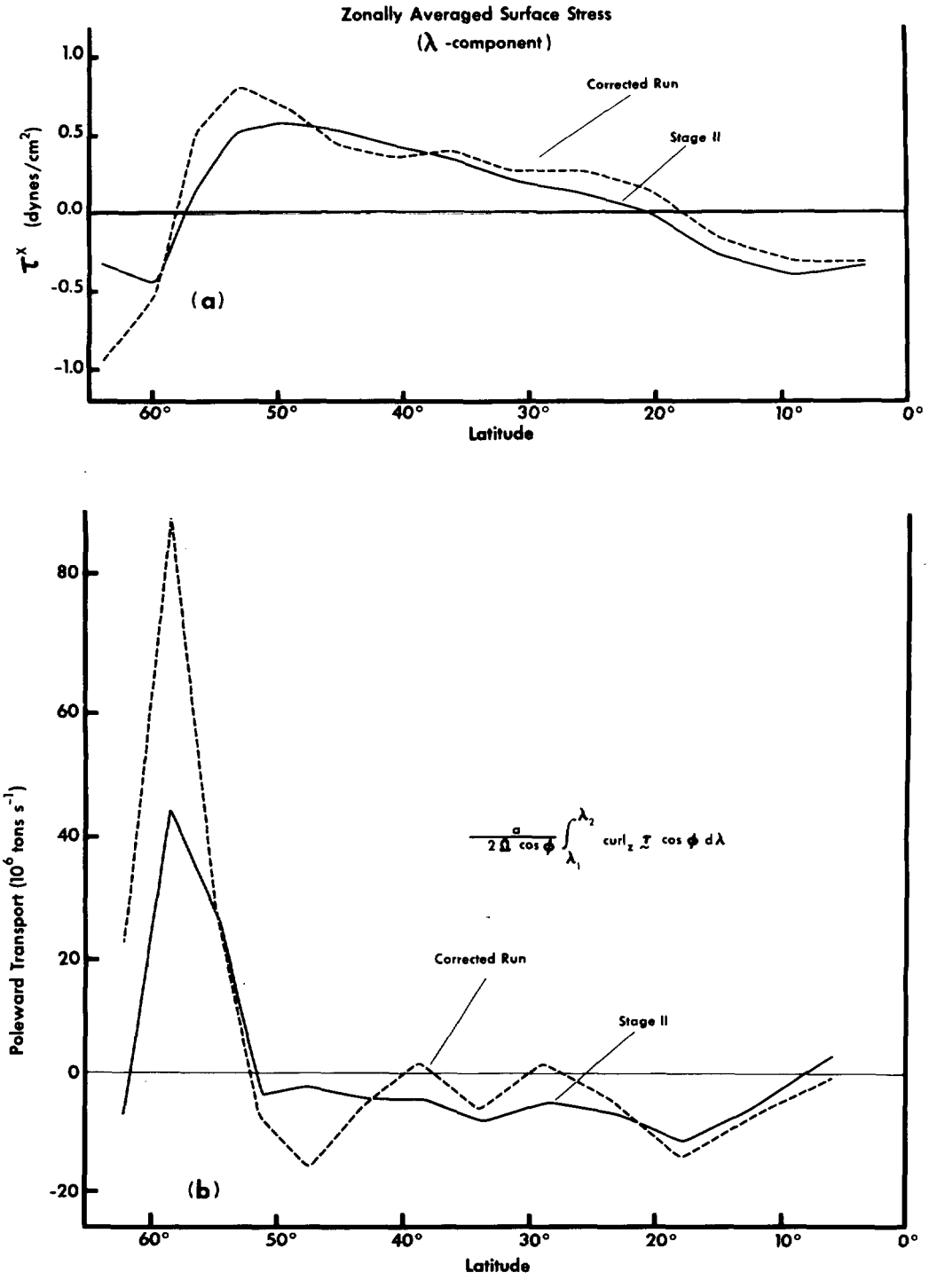

FIGURE 16.— (a) zonal average of the λ-component of the wind stress and (b) the integral of the Sverdrup transport with respect to longitude.

The average temperature over the upper 600 m of the water column is plotted as a function of time in figure 18, using a 5-yr sampling interval. Note that no sharp breaks are indicated in the average temperature curves in the transition from stage II to the corrected run. Trends that are present in stage II continue in the corrected run. While the temperature remains nearly stationary at middle latitudes, a slow warming takes place at high and low latitudes.

With regard to the large-scale interaction between the atmosphere and the ocean, the most significant process is the exchange of heat between the lower layers and the ocean surface. Zonally averaged values of this heat flux are shown in table 6. As pointed out in the appendix of

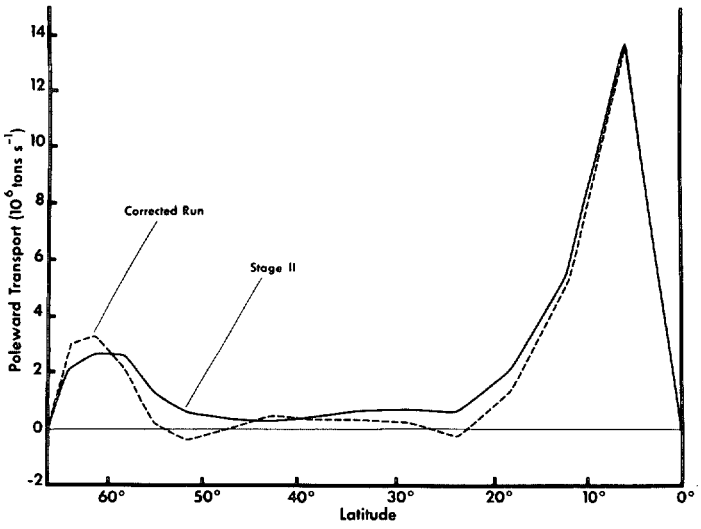

FIGURE 17.—Net poleward transport for the whole basin in the 67-m-deep layer of the model just below the surface.

TABLE 5.—*Poleward heat transport in units of 10^{14} cal sec^{-1} at various latitudes averaged for both hemispheres. The components H_1, H_2, and H_3 are defined in section 8. H_4 is the total transport. The upper row is the value corresponding to the main run and the middle row that corresponding to the extension run. The lower row is the increment for each component.*

	61°	56°	47°	38°	28°	17°	6°
H_1	0.46	0.64	1.19	1.72	1.78	1.22	0.54
	.59	.44	.98	1.51	1.59	1.05	.51
Δ	.13	—.20	—.21	—.21	—.19	—.17	—.03
H_2	—.09	.06	—.42	—.59	—.46	—.03	.07
	.00	.34	—.24	—.43	—.43	—.16	.08
Δ	.09	.28	.18	.16	.03	—.13	.01
H_3	.15	.15	.34	.22	.11	.00	.00
	.02	.15	.38	.20	.14	.05	.01
Δ	—.13	.00	.04	—.02	.03	.05	.01
H_4	.52	.85	1.11	1.35	1.43	1.19	.61
	.61	.93	1.12	1.28	1.30	.94	.60
Δ	.09	.08	.01	—.07	—.13	—.25	—.01

part II (Manabe, 1969*b*), this quantity is altered very little by the correction of the surface stress. Deviations are less than 10 percent of the maximum value. On the basis of this evidence, it is concluded that the correction of the wind stress formula does not significantly alter the climate of the joint model, relative to the overall uncertainty about the final equilibrium state caused by the persistent transients in the temperature and salinity structure of the ocean model.

ACKNOWLEDGMENTS

The author is deeply indebted to Mr. Michael D. Cox for designing the computer program for these calculations and to Lt.(jg.) David Durdall of USESSA for carrying out the calculations and assisting in analyzing the results. Miss Martha Jackson's help in preparing the figures is also deeply appreciated.

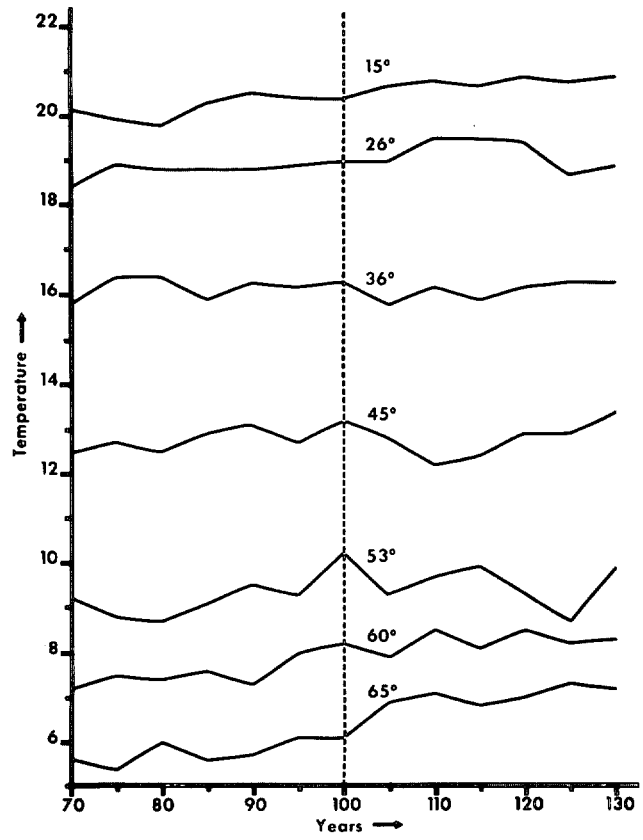

FIGURE 18.—The zonally averaged temperature trend over the upper 600 m of the model. The year 100 corresponds to the transition between stage II and the corrected run.

TABLE 6.—*Normalized and zonally averaged values of the heat transferred from lower levels in the ocean to the surface in units of 10^{-2} ly cm^{-2}*

Latitude	Main run		Corrected run	
64.0	17.5	+17.7	18.5	18.9
59.8	8.5	+8.4	7.5	8.2
56.6	6.0	+6.1	6.0	4.7
53.2	3.5	+3.2	3.0	1.7
49.4	2.5	+2.3	2.0	1.6
45.4	2.0	+2.0	1.0	1.0
41.0	1.0	+1.1	0.0	0.5
36.3	0.0	+0.3	—0.5	—0.2
31.3	—2.0	—1.7	—1.5	—0.8
26.0	—3.5	—3.5	—3.0	—1.9
20.5	—4.5	—4.6	—4.0	—4.0
14.8	—3.5	—3.6	—3.0	—3.4
8.9	—4.5	—4.5	—4.5	—4.6
3.0	—8.5	—8.6	—8.5	—8.8

REFERENCES

Albrecht, F., "Jahreskarten des Wärme- und Wasserhaushaltes der Ozeane," (Annual Charts of the heat and water balance of the oceans), *Berichte Deutscher Wetterdienst*, Vol. 9, No. 66, Germany, **1960**, pp. 3–19.

Assur, A., and Weeks, W. F., "Growth, Structure and Strength of Sea Ice," *Research Report* 135, Cold Region Research and Engineering Laboratory, Hanover, N.H., Oct. **1964**, 19 pp.

Brooks, C. E. P., *Climate Through the Ages: A Study of the Climatic Factors and Their Variations*, Benn, London, **1926**, 439 pp.

Bryan, K., "Measurements of Meridional Heat Transport by Ocean Currents," *Journal of Geophysical Research*, Vol. 67, No. 9, Aug. **1962**, pp. 3403–3414.

Bryan, K., and Cox, M. D., "A Numerical Investigation of the Oceanic General Circulation," *Tellus*, Vol. 19, No. 1, Feb. **1967**, pp. 54–80.

Bryan, K., and Cox, M. D., "A Nonlinear Model of an Ocean Driven by Wind and Differential Heating: Part I. Description of the Three-Dimensional Velocity and Density Fields," *Journal of the Atmospheric Sciences*, Vol. 25, No. 6, Nov. **1968***a*, pp. 945–967.

Bryan, K., and Cox, M. D., "A Nonlinear Model of an Ocean Driven by Wind and Differential Heating: Part II. An Analysis of the Heat, Vorticity and Energy Balance," *Journal of the Atmospheric Sciences*, Vol. 25, No. 6, Nov. **1968***b*, pp. 968–978.

Budyko, M. I., *The Heat Balance of the Earth's Surface*, (*Teplovoĭ balans zemnoĭ poverkhnosti*, 1956), N. A. Stepanova, Translator, U.S. Weather Bureau, Washington, D.C., **1958**, 259 pp.

Campbell, W. J., "The Wind-Driven Circulation of Ice and Water in a Polar Ocean," *Journal of Geophysical Research*, Vol. 70, No. 14, July 15, **1965**, pp. 3279–3301.

Eckart, C., "Properties of Water: Part 2. The Equation of State of Water and Sea Water at Low Temperatures and Pressures," *American Journal of Science*, Vol. 256, No. 4, Apr. **1958**, pp. 225–240.

Lineykin, P. S., "On the Determination of the Thickness of the Baroclinic Layer of the Sea," *Doklady Akademii, Nauk*, USSR, Vol. 101, No. 3, **1955**, pp. 461–464.

Malmgren, F., "On the Properties of Sea Ice," *Scientific Results, Norwegian North Polar Expedition With the 'Maud,' 1918-1925*, Vol. 1, No. 5, Geofysisk Institutt, Bergen, **1927**, 67 pp.

Manabe, S., "Climate and the Ocean Circulation: I. The Atmospheric Circulation and the Hydrology of the Earth's Surface," *Monthly Weather Review*, Vol. 97, No. 11, Nov. **1969***a*, pp. 739–774.

Manabe, S., "Climate and the Ocean Circulation: II. The Atmospheric Circulation and the Effect of Heat Transfer by Ocean Currents," *Monthly Weather Review*, Vol. 97, No. 11, Nov. **1969***b*, pp. 775–805.

Munk, W. H., "Abyssal Recipes," *Deep-Sea Research*, Vol. 13, No. 4, London, Aug. **1966**, pp. 707–730.

Phillips, N. A., "The General Circulation of the Atmosphere: A Numerical Experiment," *Quarterly Journal of the Royal Meteorological Society*, Vol. 82, No. 352, Apr. **1956**, pp. 123–164.

Robinson, A. R., and Stommel, H., "The Oceanic Thermocline and the Associated Thermohaline Circulation," *Tellus*, Vol. 11, No. 3, Aug. **1959**, pp. 295–308.

Saint-Guilly, B., "Sur la Théorie des Courants Marins Induits par la Vent," (On the Theory of Marine Currents Induced by the Wind), *Bulletin d'Information Central d'Oceanographie et d'Etude des Côtes*, Vol. 8, No. 3, Paris, Mar. **1956**, pp. 111–123.

Sarkisyan, A. S., "O dinamike vozniknoveniia vetrovykh techeniĭ v baroklinnom okeane," (On the Dynamics of the Origin of Wind Currents in a Baroclinic Ocean), *Okeanologiia*, Vol. 2, No. 3, Moscow, **1962**, pp. 393–409.

Smagorinsky, J., "General Circulation Experiments With the Primitive Equations: I. The Basic Experiment," *Monthly Weather Review*, Vol. 91, No. 3, Mar. **1963**, pp. 99–164.

Stommel, H., *The Gulf Stream: A Physical and Dynamical Description*, 2d Edition, University of California Press, Berkeley, **1965**, 248 pp.

Stommel, H., and Veronis, G., "Steady Convective Motion in a Horizontal Layer of Fluid Heated Uniformly From Above and Cooled Non-Uniformly From Below," *Tellus*, Vol. 9, No. 3, Aug. **1957**, pp. 401–407.

Stommel, H., and Webster, J., "Some Properties of Thermocline Equations in a Subtropical Gyre," *Journal of Marine Research*, Vol. 20, No. 1, New Haven, Conn., Mar. 15, **1962**, pp. 42–56.

Sverdrup, H. U., "Oceanography," *Handbuch der Physik*, Vol. 48, Springer-Verlag, Berlin, **1957**, pp. 608–670.

Sverdrup, H. U., Johnson, M. W., and Fleming, F. H., *The Oceans, Their Physics, Chemistry and General Biology*, Prentice-Hall, Inc., New York, **1942**, 1087 pp.

Untersteiner, N., "Calculations of Temperature Regime and Heat Budget of Sea Ice in the Central Arctic," *Journal of Geophysical Research*, Vol. 69, No. 22, Nov. 15, **1964**, pp. 4755–4766.

Veronis, G., and Stommel, H., "The Action of Variable Wind Stresses on a Stratified Ocean," *Journal of Marine Research*, Vol. 15, No. 1, New Haven, Conn., Oct. **1956**, pp. 43–75.

Welander, P., "An Advective Model of the Ocean Thermocline," *Tellus*, Vol. 11, No. 3, Aug. **1959**, pp. 309-318.

[*Received February 3, 1969; revised August 8, 1969*]